Cell Reports

Article

Fasting renders immunotherapy effective against low-immunogenic breast cancer while reducing side effects

Graphical abstract

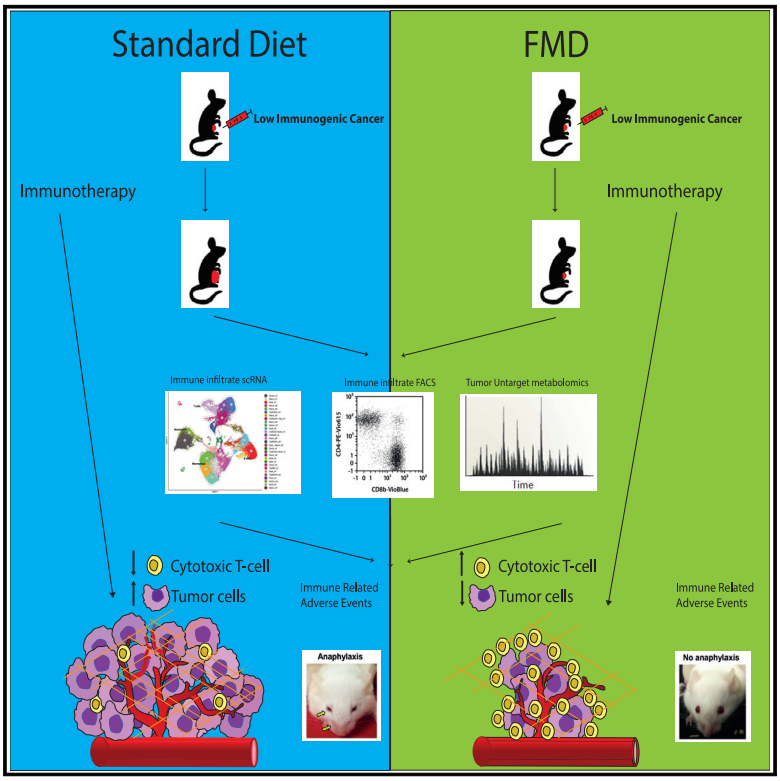

Highlights

- FMD improves the efficacy of immunotherapy against triple-negative breast cancer
- FMD increases the percentage of early exhausted effector T cells
- FMD reduces intratumor collagen deposition, a poor-prognosis marker
- FMD prevents immunotherapy side effects

Authors

Salvatore Cortellino, Alessandro Raveane, Claudia Chiodoni, ..., Mario P. Colombo, Claudio Tripodo, Valter D. Longo

Correspondence

vlongo@usc.edu, valter.longo@ifom.eu

In brief

Cortellino et al. show that FMD sensitizes low-immunogenic and poorly responsive triple-negative breast cancer to immunotherapy, so it could be tested in a clinical trial in cancer patients to determine whether it improves their prognosis. Furthermore, the authors demonstrate that FMD reduces the adverse side effects associated with immunotherapy.

Cortellino et al., 2022, Cell Reports *40*, 111256
August 23, 2022
https://doi.org/10.1016/j.celrep.2022.111256

CellPress

Cell Reports

CellPress
OPEN ACCESS

Article

Fasting renders immunotherapy effective against low-immunogenic breast cancer while reducing side effects

Salvatore Cortellino,[1] Alessandro Raveane,[2,8] Claudia Chiodoni,[3] Gloria Delfanti,[4] Federica Pisati,[1] Vanessa Spagnolo,[1] Euplio Visco,[1] Giuseppe Fragale,[1] Federica Ferrante,[1] Serena Magni,[1] Fabio Iannelli,[1] Federica Zanardi,[1] Giulia Casorati,[4] Francesco Bertolini,[2,6] Paolo Dellabona,[4] Mario P. Colombo,[3] Claudio Tripodo,[1,5] and Valter D. Longo[1,7,9,*]

[1]IFOM, FIRC Institute of Molecular Oncology, Milan 20139, Italy
[2]Laboratory of Hematology-Oncology, European Institute of Oncology IRCCS, Milan 20141, Italy
[3]Department of Research, Fondazione IRCCS Istituto Nazionale Tumori, Milan, Italy
[4]Experimental Immunology Unit, Division of Immunology, Transplantation and Infectious Diseases, IRCCS San Raffaele Scientific Institute, Milan, Italy
[5]University of Palermo School of Medicine, Palermo, Italy
[6]Onco-Tech Lab, European Institute of Oncology IRCCS and Politecnico di Milano, Milan, Italy
[7]Longevity Institute and Davis School of Gerontology, University of Southern California, Los Angeles, CA 90089, USA
[8]Present address: Human Technopole, Milan, Italy
[9]Lead contact
*Correspondence: vlongo@usc.edu or valter.longo@ifom.eu
https://doi.org/10.1016/j.celrep.2022.111256

SUMMARY

Immunotherapy is improving the prognosis and survival of cancer patients, but despite encouraging outcomes in different cancers, the majority of tumors are resistant to it, and the immunotherapy combinations are often accompanied by severe side effects. Here, we show that a periodic fasting-mimicking diet (FMD) can act on the tumor microenvironment and increase the efficacy of immunotherapy (anti-PD-L1 and anti-OX40) against the poorly immunogenic triple-negative breast tumors (TNBCs) by expanding early exhausted effector T cells, switching the cancer metabolism from glycolytic to respiratory, and reducing collagen deposition. Furthermore, FMD reduces the occurrence of immune-related adverse events (irAEs) by preventing the hyperactivation of the immune response. These results indicate that FMD cycles have the potential to enhance the efficacy of anti-cancer immune responses, expand the portion of tumors sensitive to immunotherapy, and reduce its side effects.

INTRODUCTION

Immunotherapy has yielded very positive results in the treatment of melanoma, lung, and colorectal cancer, but most patients are refractory to the treatment, and its effectiveness is thus far limited to specific cancer types.

Activated T cells express the immune checkpoint programmed cell death protein (PD-1), cytotoxic T lymphocyte antigen 4 (CTLA-4), and the costimulatory receptor OX40 and induce the expression of the immune checkpoint programmed death ligand 1 (PD-L1) on tumor cells. The binding of PD-1 with PD-L1 and CTLA4 with B7, expressed by macrophages and dendritic cells, inhibits activated T cells and leads to T cell exhaustion, allowing tumor cells to evade immune system attack (Wei et al., 2018), whereas the interaction of OX40 with its ligand OX40L, expressed by activated B cells (Stuber et al., 1995), endothelial cells, dendritic cells, and activated macrophages (Imura et al., 1996), enhances T cell proliferation, cytokine production, and effector T cell survival (Flynn et al., 1998; Ohshima et al., 1998).

Cancer cells also promote an immune-suppressive microenvironment by secreting pro-inflammatory cytokines and chemokines that recruit tumor-associated macrophages (TAMs) and myeloid-derived suppressor cells (MDSCs), which act as major barriers to the cancer immune response and immunotherapy (Bayne et al., 2012; Zhu et al., 2014).

Immune checkpoint inhibitors, such as antagonist antibodies against PD-1, PD-L1 or CTLA4, and costimulatory receptors or agonist antibody against OX40, were found to have good clinical responses in some immunogenic tumors, but to be inefficient toward so-called immunoprivileged tumors (Herbst et al., 2014; Topalian et al., 2012; Kjaergaard et al., 2000; Weinberg et al., 2000; Gough et al., 2008; Piconese et al., 2008). The combination therapy of an anti-PD-1 antagonist and anti-OX40 agonist has led to conflicting results based on the type of tumor in several preclinical studies (Shrimali et al., 2017; Messenheimer et al., 2017; Ma et al., 2020).

Notably, immunotherapy and, even more so, the combination of immunotherapeutics increase the risk of adverse events, which limits their application in the clinic (Suntharalingam

et al., 2006; Lee et al., 2009; Topalian et al., 2012; Brahmer et al., 2012).

In the past decade it has emerged that the use of a nutritional composition mimicking the effects of fasting, or fasting-mimicking diet (FMD), promotes rejuvenating effects on the immune system and synergizes with chemotherapy, radiotherapy, hormone therapy, and tyrosine kinase inhibitors to induce better anti-tumor response in both mice and humans and, in some cases, has led to complete tumor eradication in preclinical tumor models (Raffaghello et al., 2008; Lee et al., 2012; Cheng et al., 2014; Brandhorst et al., 2015; Wei et al., 2017; Nencioni et al., 2018; de Groot et al., 2020; Caffa et al., 2020; Weng et al., 2020).

More recently, we and others have shown that fasting/FMD promotes the immune cell-dependent attack of different types of cancer cells, by stimulating CD8 infiltration into tumors (Di Biase et al., 2016; Ajona et al., 2020; Pietrocola et al., 2016).

Here we investigated the effects of FMD cycles on the toxicity of anti-OX40 and anti-PD-L1 against low-immunogenic triple-negative breast cancer models.

RESULTS

FMD in combination with anti-OX40/anti-PD-L1 inhibits the growth of breast (4T1) cancer

Mice bearing 4T1 breast cancer cells orthotopically implanted in the mammary fat pad were subjected to two cycles of a 4-day FMD and treated with three doses of anti-OX40 and anti-PD-L1, alone or in combination (Figure 1A). In the control group, treated with IgG only, FMD alone inhibits tumor growth compared with the standard diet group (*ad libitum*, AL), while anti-PD-L1 monotherapy does not provide any anti-tumor benefit in either the AL or the FMD group. Anti-OX40 treatment has no anti-tumoral effect in mice fed a standard diet, while delaying tumor growth in mice fed FMD (Figures 1B and 1C).

The sequential combination of the anti-OX40/anti-PD-L1 treatment reduces the tumor masses in the standard diet group but is much more effective in combination with FMD (Figures 1B and 1C). FMD + immunotherapy extends mouse survival significantly more than the other treatments. Mice survive up to 26 days in the untreated groups or standard diet + immunotherapy, whereas FMD + immunotherapy extends mouse survival up to 33 days. Therefore, FMD + immunotherapy, but not immunotherapy alone, slows tumor growth and increases survival (Figure S1A).

In addition, FMD reduces splenomegaly in the anti-OX40/anti-PD-L1 treatment group (Figure 1D). Enlarged spleen might be a consequence of an increased myelopoiesis at the expense of erythropoiesis and lymphopoiesis and accumulation of exhausted lymphocytes (Messenheimer et al., 2017).

To establish the role of the immune system in these effects, the same treatment scheme was performed in NSG immunodeficient mice bearing 4T1 tumors. Although FMD alone has a negligible effect on the tumor growth inhibition, the combined anti-OX40/anti-PD-L1 therapy is no longer effective in immunodeficient mice, suggesting that the anti-tumor effects of FMD + anti-OX40/anti-PD-L1 are mediated by the immune system (Figures 1E and 1F).

Single-cell transcriptomic analysis reveals that FMD combined with anti-OX40 or anti-OX40/anti-PD-L1 boosts anti-tumoral response by promoting T cell activation

To determine how FMD increases the anti-tumor efficacy of anti-OX40 and anti-PD-L1 therapy against breast cancer, we performed single-cell RNA sequencing (scRNA-seq) on $CD45^+$ tumor-infiltrating leukocytes isolated from 4T1 breast cancer harvested 3 days after the second cycle of FMD. The 10X Genomics Chromium platform (Zheng et al., 2017) was employed to sequence ~10,000 tumor-derived $CD45^+$ immune cells obtained from two biological replicates for each group (AL IgG, FMD IgG, AL anti-OX40/anti-PD-L1, FMD anti-OX40/anti-PD-L1).

Using a graph-based clustering of uniform manifold approximation and projection (UMAP), we identified 29 clusters (Figure S2A). These clusters were assigned to cell populations using a known gene marker-based manual curation and a specific reference-based scRNA-seq annotation (SingleR). The classification resulted as follows: seven macrophage/monocyte clusters (high expression of *Cd68*, *Mrc1*, and *Adgre1* markers), six B cell clusters (high expression of *Cd19* marker), three granulocyte/monocyte clusters (high expression of *Cd68* and *Csf3r* markers), eight T/natural killer (NK) cell clusters (high expression of *Cd3e*, *Cd4*, *Cd8a*, and *Ncr1* markers), and two dendritic clusters (high expression of *Basp1* marker). Of these, we identified four main macroclusters named T cells, neutrophils, B cells, and macrophages according to the specific gene expression mentioned above (Figure S2B).

Then we calculated the relative percentages of cells in each of the 29 clusters for each condition, and T cell clusters associated with potential regulatory (cluster 7) and cytotoxic (clusters 11 and 22) activities were found to be highly enriched in FMD with combined immunotherapy compared with the other groups (Figure S2C). No major differences were found in the number of cells belonging to the myeloid clusters, except for a macrophage cluster (cluster 6), which was mainly enriched in FMD treatments (Figure S2C).

To further investigate the differences observed in T cell clusters, we performed a new clustering analysis on a subset of cells belonging to all the clusters under the macrogroup named "T cells" in Figure S2A. Graph-based clustering identified 14 subclusters, which were assigned specific names according to the expression of known gene markers (Wisdom et al., 2020) (Figures 2A, 2B, and S2D). The resulting subclusters included three CD4-CD8 mixed T cell clusters (0, 1, 3) (high expression of *Cd3d*, *Cd4*, *Cd8a*, and *Tcf7*), comprising naive and memory T cells; a CD4 T cell cluster (2) (high expression of *Cd3d* and *Cd4*; *Foxp3* negative expression); an activated CD8 T cell cluster (5) (high expression of *Cd8a*, *GzmB*, *Lag3* and *Pdcd1)*; an NK cell cluster (6) (high expression of *Ncr1* and *GzmB*); a regulatory T cell cluster (7) (high expression of *Cd4* and *Foxp3*); two ISG CD4-CD8 T cell clusters (8, 12) (high expression of interferon-stimulated genes such as *Isg15*); a $Ki67^+$CD4-CD8 T cell cluster (9) (high expression of proliferating marker Ki67); and a $\gamma\delta$ T cell cluster (10) (high expression of *Cd3d* and *Trdc*) (Figures 2B and S2D).

The analysis of the top 20 upregulated differentially expressed genes (DEGs) from each cluster delineated a specific RNA signature for each subcluster of T cells (Figure S2D). Three clusters

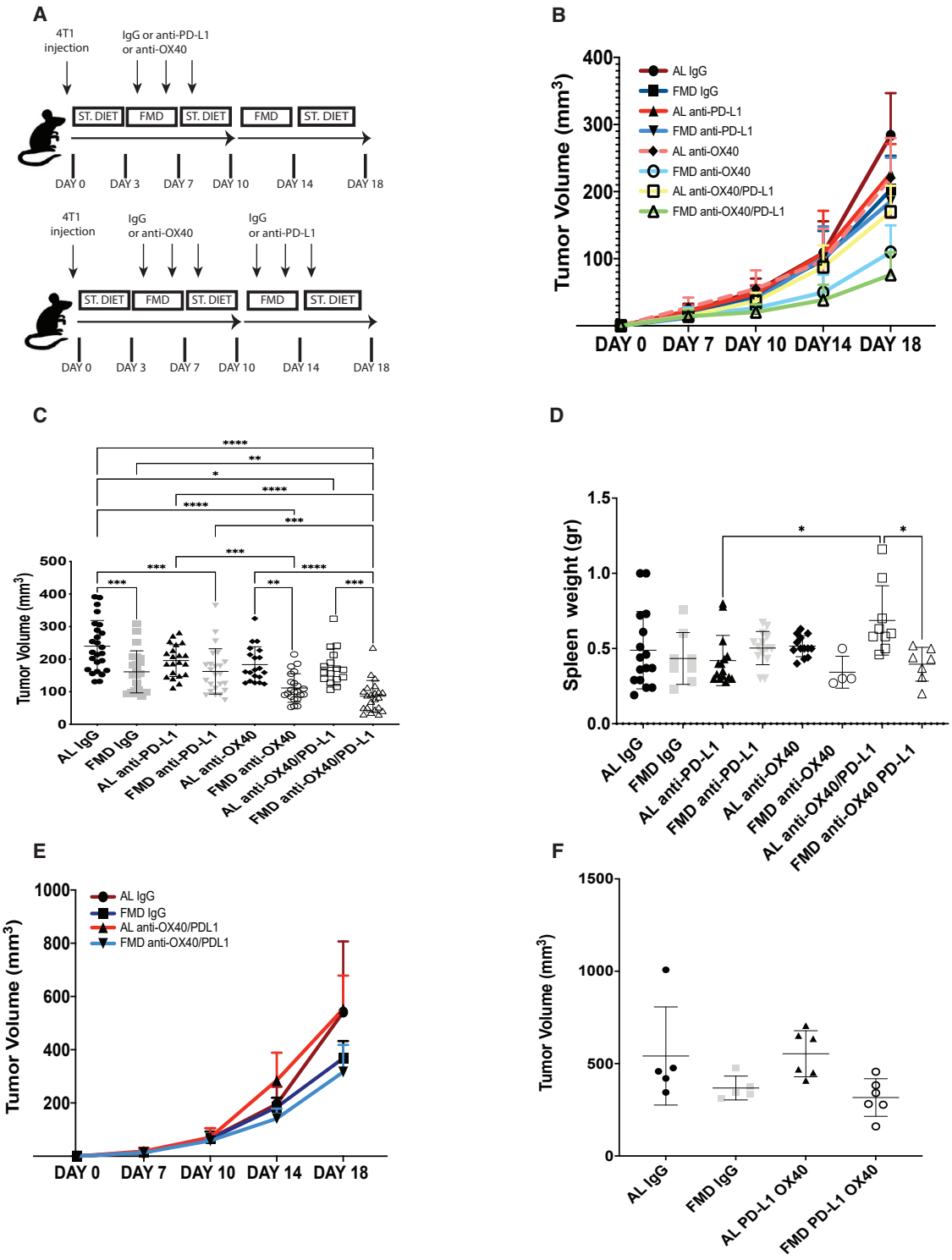

Figure 1. FMD enhances the efficacy of anti-OX40/anti-PD-L1 combined treatment against 4T1 breast tumor

(A) Schedule of tumor implantation and treatment for 4T1 syngeneic orthotopic tumor models.

(B and C) 4T1 tumor growth in immunocompetent BALB/c syngeneic mice treated with isotype control, anti-OX40, and anti-PD-L1 and fed with standard diet or FMD (n = 20–25).

(D) Spleen size of 4T1 tumor-bearing mice collected at the last day of FMD, 3 days after refeeding, or during the standard diet (n = 4–16).

(E and F) Tumor growth in immunodeficient NSG mice treated with isotype control, anti-OX40, and anti-PD-L1 and fed with standard diet or FMD (n = 5). The p values from two-way analysis of variance (ANOVA) were *p < 0.05, **p < 0.005, ***p < 0.0005, and ****p < 0.0001.

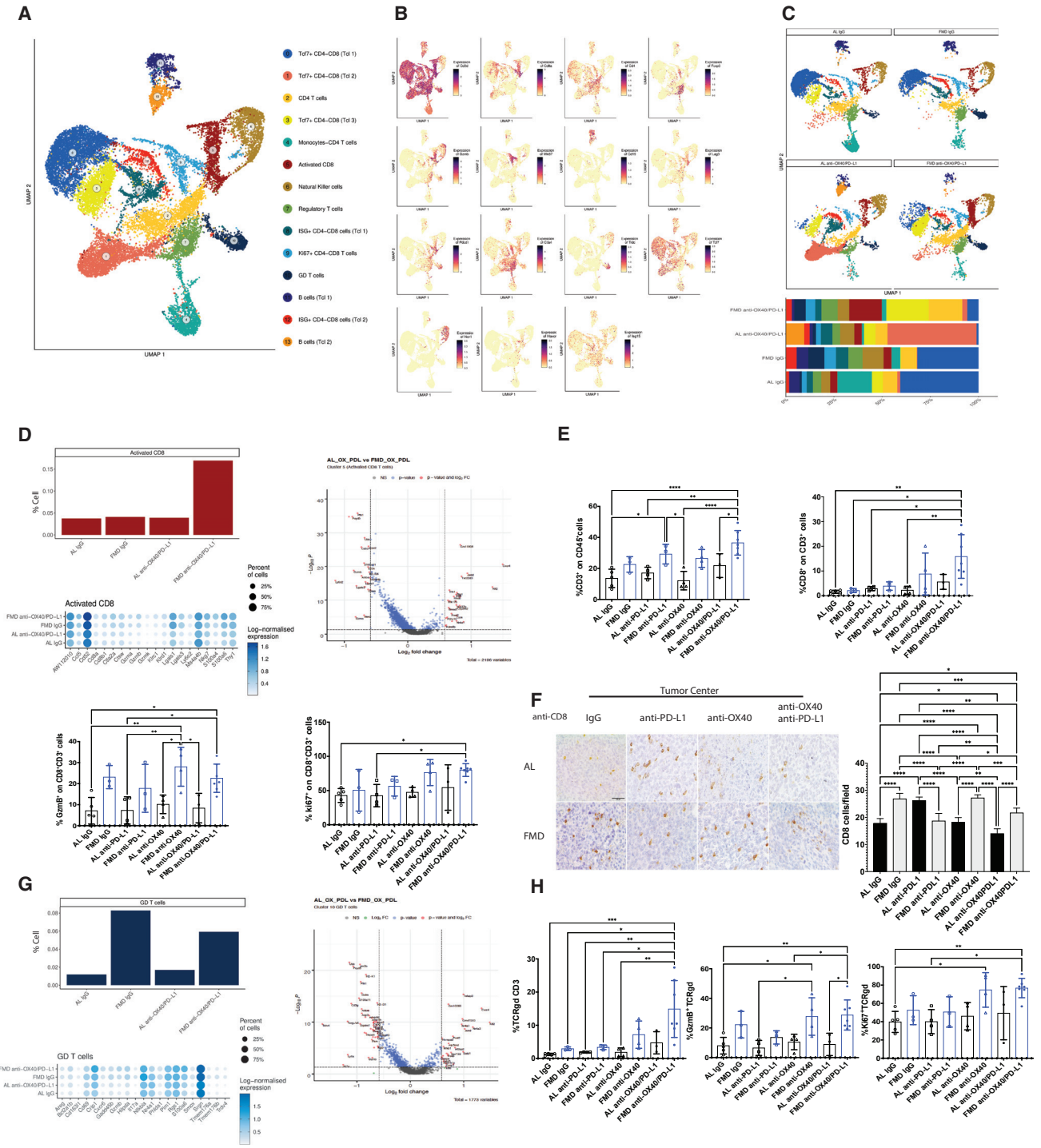

Figure 2. FMD + immunotherapy promotes T lymphocyte activation and differentiation

(A) t-distributed stochastic neighbor embedding (t-SNE) plot of $CD3^+$ T lymphocyte infiltrate scRNA-seq subclustering from standard and FMD group plus treatment (n = 2).

(B) Expression of marker genes.

(C) Cluster percentage of immune cells from standard and FMD group plus treatment.

(D) Percentages of activated CD8 T cells from individual experimental groups. Dot plot of the top 20 differentially expressed genes defining the activated $CD8^+$ T cell cluster. Intensity of blue color indicates the normalized level of gene expression, and the size of the dot represents the percentage of cells expressing that gene. Volcano plot depicts differentially expressed genes in FMD anti-OX40/anti-PD-L1 versus AL anti-OX40/anti-PD-L1.

(legend continued on next page)

were not considered in further analyses because they were associated with monocytes (cluster 4) and B cells (clusters 11 and 13).

Activated CD8 T cells, γδ T cells, and CD4 conventional and regulatory T (Treg) cells were confirmed to be the most enriched in the FMD + immunotherapy group compared with all the other experimental conditions (Figure 2C).

Cells belonging to the activated CD8 cluster (cluster 5) express high levels of *Ccl5*, *Cd52*, *Ctla2a*, *GzmB*, and *GzmK*, which are upregulated genes in the differentiated cytotoxic CD8 T cells (Figure 2D). The FMD + immunotherapy increases the expression of genes associated with the cytotoxic activity and the percentage of activated CD8 T cells in the tumor immune infiltrate compared with the other experimental groups (Figure 2D). Several genes involved in the negative modulation of cytotoxic T cell differentiation and activity, such as *Smad7*, *Klf2*, *Jund*, *Cxcr4*, and *Nr4a1*, were significantly downregulated in FMD + immunotherapy group compared with the standard diet + immunotherapy group on cluster 5 (Figure 2D).

Then, we analyzed the immune infiltrate by fluorescence-activated cell sorting (FACS) to confirm scRNA data at the protein level. FMD alone or in combination with immunotherapy increases CD3 T lymphocyte infiltration (Figure 2E), whereas only the combination FMD + anti-OX40 or anti-OX40/anti-PD-L1 promotes tumor CD8 T cell infiltration (Figure 2E). In accordance with the single-cell gene expression profile (Figure 2D), FMD alone promotes CD8 cytotoxic T cell activation and differentiation. Indeed, the percentage of $GzmB^+CD8^+$ T cell is consistently and significantly higher in the FMD groups compared with the standard diet groups (Figure 2E). The combination of FMD with anti-OX40 or anti-OX40/anti-PD-L1 leads to an increased CD8 T cell proliferation ($Ki67^+CD8^+$) (Figure 2E). Immunohistological characterization of CD8 T lymphocytes on the tumor sections also showed that FMD alone or in combination with anti-OX40 and anti-PD-L1/anti-OX40 increases activated CD8 T lymphocyte accumulation and infiltration in the tumor central area compared with standard diet groups (Figure 2F). Since FMD increases $Ki\text{-}67^+$ tumor-infiltrating lymphocytes (TILs), the intratumor expansion of activated CD8 T cells may also result from a local proliferation.

scRNA-seq analysis also revealed that FMD increases the percentage of the γδ T cell cluster (cluster 10) population in the immune infiltrate (Figure 2G). This cluster is enriched for genes such as *Areg*, *Scart1*, *Cxcr6*, and *Il17a* (Figures 2G and S2D), which are normally expressed in γδ T cell populations (Tan et al., 2019) (Figure 2G). High expression of the *Trdv4* gene in this cluster suggests that the Vδ1 cell subtype is the main population (Figure 2G). γδ T cells can exert a strong anti-tumor function in several cancer models (Silva-Santos et al., 2019). In our experiment, FMD increased the percentage of Vδ1 γδ T cell infiltration and skewed them toward cytolysis and *Gzmb* production (dot plot, Figure 2G). Genes involved in glycolysis and glutathione metabolism, such as *Aldoa*, *Pkm*, and *Gclm*, essential for cytotoxic activity of γδ T cells, were also found to be upregulated in FMD + anti-OX40/anti-PD-L1 (volcano plot, Figure 2G). On the other hand, immunotherapy alone increased the expression levels of the genes involved in the inhibition of T cell activation, such as *Jund*, *Nr4a1*, *Cxcr4*, and *Klf2*. FACS analysis confirmed that FMD in combination with immunotherapy increases the percentage of γδ T cells ($TCR\gamma\delta^+CD3$) in the immune infiltrate and promotes their activation and differentiation into cytotoxic T cells ($GzmB^+Tcr\gamma\delta$) and their proliferation ($Ki67^+TCR\gamma\delta$) (Figure 2H).

CD4 T cells play an important role in the immune response and orchestrate anti-tumor immunity by supporting the induction and clonal expansion of the cytotoxic CD8 T cell response (Richardson et al., 2021). Our scRNA experiment revealed a CD4 T cell expansion in FMD + anti-OX40/anti-PD-L1. The conventional CD4 T cell cluster was characterized by the expression of genes involved in T cell activation, such as *Bhlhe40*, *Ifitm2*, *Itgb1*, *Tnf18*, and *Tnfrsf4* (*Ox40*) (Figures 3A and S2D). The percentage of activated conventional T cells was higher in the FMD group than in the standard diet groups, as shown in the dot plot (Figure 3A), but there were no significant differences in gene expression between the FMD group and the standard diet group treated with immunotherapy, except for four genes (Figure 3B). Unlike scRNA data, FACS analysis of the immune infiltrate did not detect differences in CD4 T cells (CD4) and conventional T cells ($FoxP3^-CD4$) (Figure S2E). However, FMD in combination with anti-OX40 or anti-OX40/anti-PD-L1 promoted the proliferation of conventional CD4 T cells ($Ki67^+FoxP3^-CD4$) and their activation ($OX40^+$ $FoxP3^-CD4$ and $PD1^+FoxP3^-CD4$) (Figure 3C), as observed in the scRNA and shown in the dot plot (Figure 3A).

Finally, the population of the Treg cell cluster (cluster 7), characterized by the expression of regulatory genes such as *Ctla4*, *Foxp3*, *Icos*, *Id2*, *Il2ra*, *Ly6a*, *Tigit*, and *Tnfrsf4/9/18*, was higher in the FMD IgG and FMD anti-OX40/anti-PD-L1 groups compared with standard diet groups (Figure S2F). The dot plot and volcano plot indicated that many of these genes were more expressed in the FMD IgG and FMD + immunotherapy groups compared with the other conditions (Figure S2F). FACS analysis of the tumor immune infiltrate did not reveal any difference in the percentage of Tregs between the different experimental groups (Figure S2G). However, FMD alone, but especially in combination with anti-OX40 and anti-OX40/anti-PD-L1, increased the percentage of proliferating and $OX40^+$ Tregs ($Ki67^+FoxP3^+CD4$, $OX40^+$ $FoxP3^+CD4$) compared with the standard diet groups (Figure S2G). scRNA analysis also confirmed that *Tnfrsf4* (*Ox40*), a gene marker of activation, was highly expressed in the Tregs of the FMD + immunotherapy group (Figure S2G). No differences were observed in the various experimental groups regarding the expression of *Pd1* (*Pdcd1*) (Figure S2G). The increase in the $OX40^+$ Treg percentage may be due to the need to modulate

(E) FACS analysis of tumor $\%CD3^+$ on $CD45^+$ cells, $\%CD8^+$ on $CD3^+$ cells, $\%GzmB^+$ on $CD8^+CD3^+$ cells, and $\%ki67^+$ on $CD8^+CD3^+$ cells (n = 3–6).
(F) CD8 immunostaining and quantitative analysis in central tumor area (n = 5).
(G) Percentage of γδ T cells from individual experimental groups (n = 2). Dot plot of the top 20 differentially expressed genes defining the $\gamma\delta^+$ T cell cluster. Intensity of blue color indicates the normalized level of gene expression, and the size of the dot represents the percentage of cells expressing that gene. Volcano plot depicts differentially expressed genes in FMD anti-OX40/anti-PD-L1 versus AL anti-OX40/anti-PD-L1 (n = 3–6).
(H) FACS analysis of tumor $CD45^+CD3^+TCR\gamma\delta^+$, $CD45^+CD3^+TCR\gamma\delta^+GzmB^+$, and $CD45^+CD3^+TCR\gamma\delta^+Ki67^+$ frequency. The p values from two-way ANOVA were $^*p < 0.05$, $^{**}p < 0.005$, $^{***}p < 0.0005$, and $^{****}p < 0.0001$.

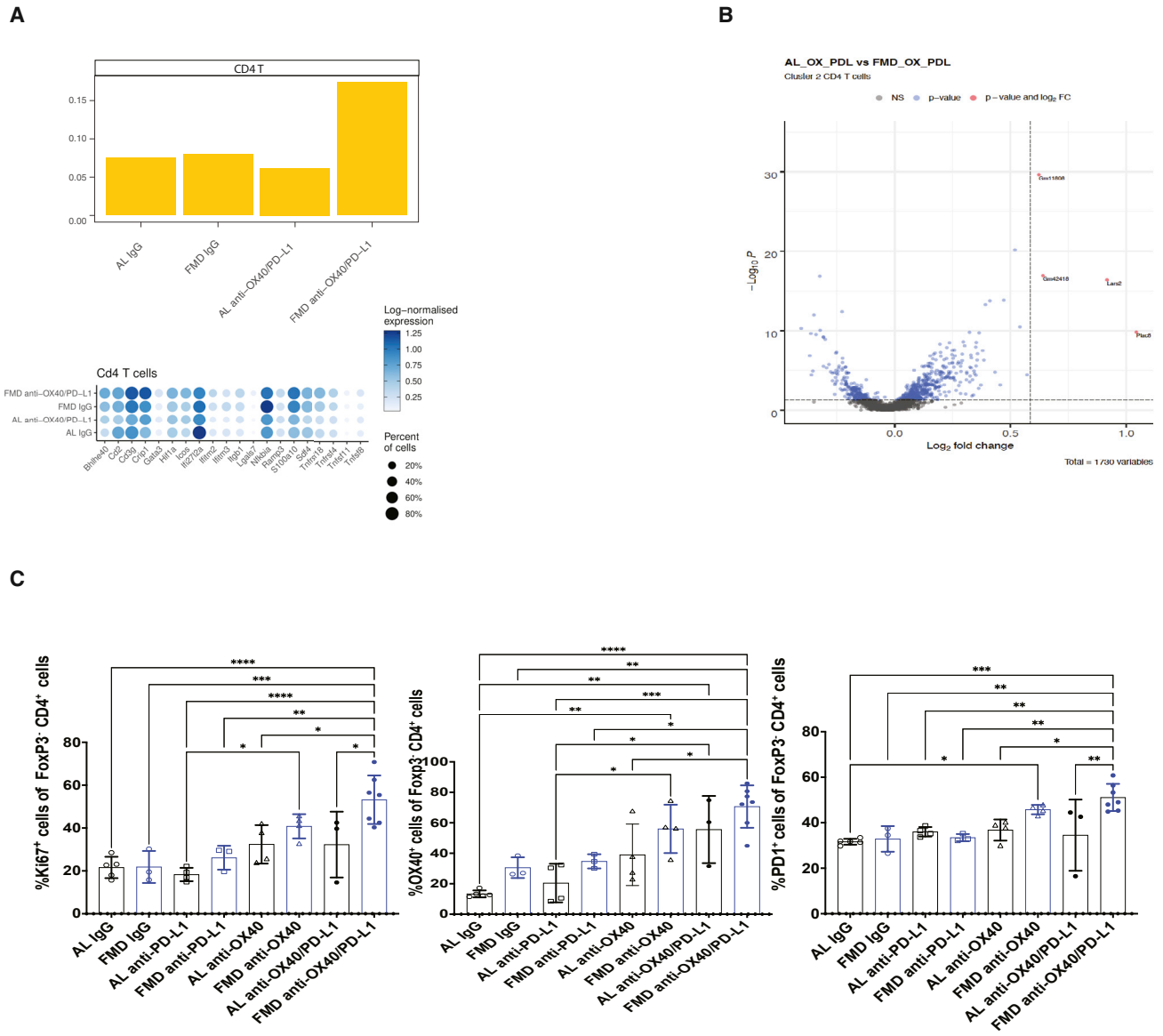

Figure 3. FMD + immunotherapy modulates conventional and regulatory T cell activation

(A) Percentage of activated CD4 T cells from individual experimental groups. Dot plot of the top 20 differentially expressed genes defining a $CD4^+$ T cell cluster. Intensity of blue color indicates the normalized level of gene expression, and the size of the dot represents the percentage of cells expressing that gene (n = 2).

(B) Volcano plot depicting differentially expressed genes in FMD anti-OX40/anti-PD-L1 versus AL anti-OX40/anti-PD-L1.

(C) FACS analysis of tumor %$Ki67^+$ cells of $FOXP3^-CD4^+$ cells, %$OX40^+$ cells of $FOXP3^-CD4^+$ cells, and %$PD1^+$ cells of $FOXP3^-CD4^+$ cells (n = 3–6). The p values from two-way ANOVA were *p < 0.05, **p < 0.005, ***p < 0.0005, and ****p < 0.0001.

the cytotoxic activity of lymphocytes to control the activation of the immune response in the FMD group.

In summary, this scRNA and FACS analysis of immune infiltrate confirmed that FMD + immunotherapy increases CD8, CD4, and γδ T cell activation.

FMD shapes the innate immune system to promote anti-tumor immunity

Since the depletion of MDSCs has been shown to markedly enhance the efficacy of immunotherapy (Kim et al., 2014; Krishnamoorthy et al., 2021), we explored whether FMD + immunotherapy modulates MDSCs and other innate immune cell populations.

To dissect the heterogeneous composition of granulocytes infiltrating the tumor, we filtered and subclustered all the cells belonging to the macrocluster named neutrophils (Figure S2A) that expressed the granulocyte colony-stimulating factor receptor (*Csf3r*), a receptor specific for neutrophil lineages. This analysis revealed eight neutrophil clusters (Figure 4A) representing immature neutrophils (*Arg2*, *Il1b*, *Nfkbia*, *Fgcr3*) (Xie et al., 2020) and characterized by poor expression of marker genes associated with mature neutrophils (*Gm2a*, *Fgl2*, *Gntg2*, *Mmp8*). However, we

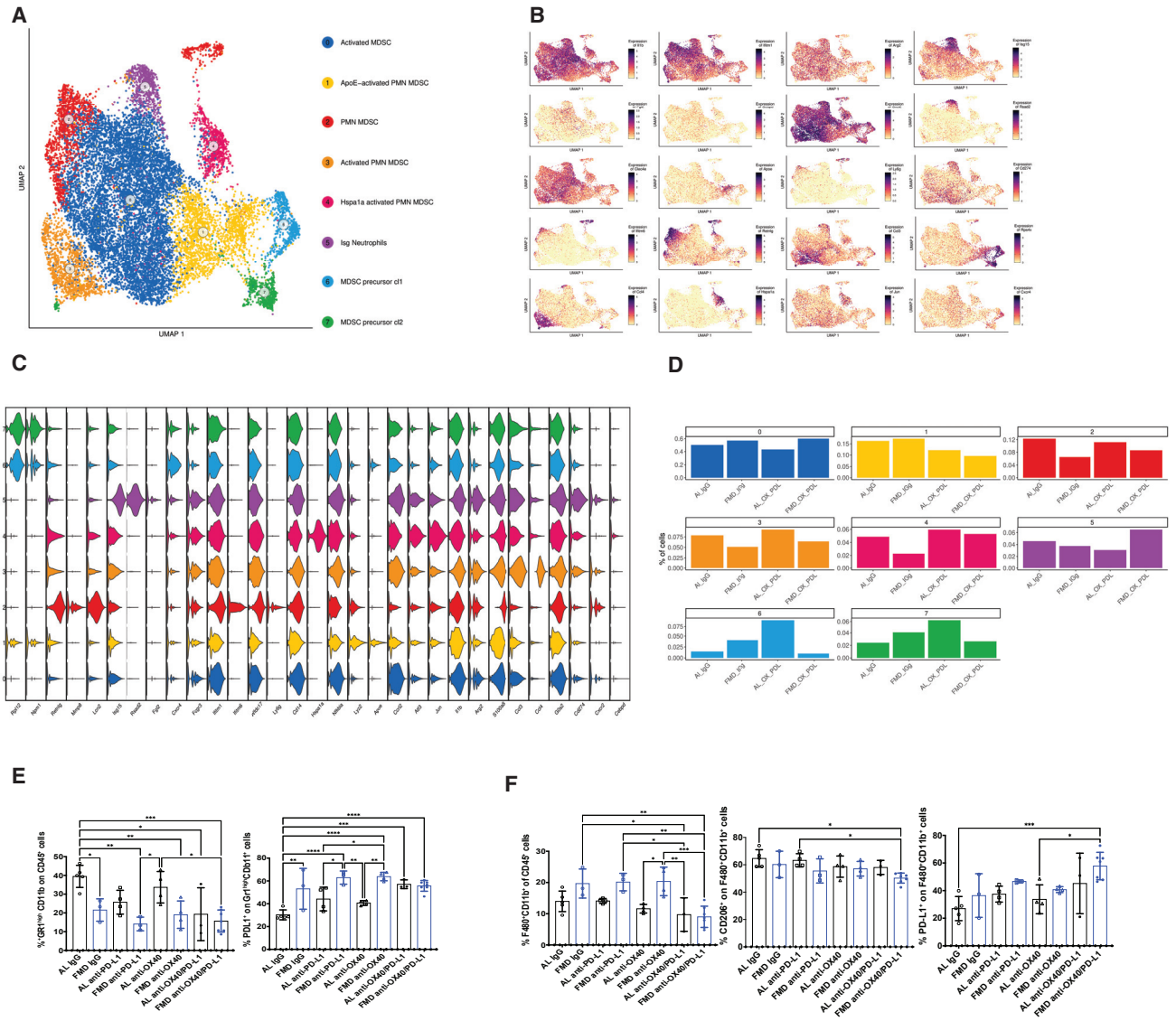

Figure 4. FMD reduces immunosuppressive PMN-MDSCs in immune infiltrate

(A) Two-dimensional UMAP embedding of "Neutrophils" macrogroup cells (Figure S1C) colored according to the clusters (subclusters) (n = 2).

(B) Expression of marker genes.

(C) Violin plots of genes with differential expression (rows) among the granulocyte cell cluster (n = 2).

(D) Cluster percentage of immune cells from standard and FMD groups plus treatment (n = 2).

(E) FACS analysis of PMN-MDSCs, %$Gr1^{high}CD11b^{+}$ on $CD45^{+}$ cells and %$PDL1^{+}$ on $Gr1^{high}CD11b^{+}$ cells (n = 3–6).

(F) FACS analysis of macrophages, %$F480^{+}CD11b^{+}$ of $CD45^{+}$ cells, %$CD206^{+}$ on $F480^{+}CD11b^{+}$ cells, and %PD-$L1^{+}$ on $F480^{+}CD11b^{+}$ cells (n = 3–6). The p values from two-way ANOVA were *p < 0.05, **p < 0.005, ***p < 0.0005, and ****p < 0.0001.

were able to classify these clusters into three groups: classic PMN-MDSCs, activated PMN-MDSCs, and precursor MDSCs. The classic PMN-MDSCs are represented by the cells of cluster 2 (*Ly6g*, *S1008a*, *Lcn2*, *Retnlg*), while the activated PMN-MDSCs included several clusters (0, 3, 4, 5) that were characterized by the overexpression of specific genes. Cluster 0 displayed high expression of activation gene markers such as *Cxcl3*, *Cxcl2*, and *Clec4e*; cluster 1 highly expressed *Apoe* and *Cd74*; cluster 3 expressed activation markers such as *Ccl3* and *Ccl4*; cluster 4 was enriched in the expression of genes involved in stress, such as *Hspa1*, *Atf3*, and *Jun*; whereas cluster 5 was characterized by the expression of genes stimulated by interferon, such as *Isg15*, *Ifi47*, *Cd274* (*Pdl1*), and *Rsad2*. Clusters 6 and 7 have been classified as MDSC precursors as they express high levels of *Rpl12* and *Npm1* genes (Figures 4B and 4C). The relative cell frequency of each cluster in each condition showed that FMD alone reduced the cell number of PMN-MDSCs (cluster 2) and activated PMN-MDSCs (clusters 3–4). FMD in combination with anti-OX40/anti-PD-L1 caused a slight reduction of PMN-MDSCs (cluster 2), activated PMN-MDSCs (clusters 1 and 3), and caused

greater cell depletion of MDSC precursors (clusters 6–7). In addition, FMD + immunotherapy increased the ISG PMN-MDSC population (cluster 5), probably due to a greater inflammatory response within the tumor bed (Figure 4D).

We then analyzed the PMN-MDSCs ($GR1^{high}CD11b^{+}$) of the tumor immune infiltrate by FACS. As observed in the scRNA analysis, FMD reduced the percentage of PMN-MDSCs in the immune infiltrate and at the same time induced a higher expression of PD-L1, which could be dependent on a high inflammatory response and IFNγ release in the FMD groups (Figure 4E).

There were no differences in the populations of monocytic MDSCs (M-MDSCs) in the various experimental groups (Figure S2H), while there was a significant increase in tumor-infiltrating macrophages in the FMD groups, with the exception of the FMD + anti-OX40/anti-PD-L1 immunotherapy group, where there was a marked reduction in the macrophage population. However, FMD did not affect the polarization of macrophages ($CD206^{+}F4/80^{+}$), although, in combination with anti-OX40/anti-PD-L1, it decreased M2 polarized macrophages compared with the standard diet plus IgG or anti-PD-L1 and induced high expression of PD-L1 ($F4/80^{+}$ $PD\text{-}L1^{+}$) (Figure 4F).

FMD remodels the tumor stroma and normalizes tumor vasculature

Since high collagen deposition in breast cancer promotes tumor development and progression and is usually linked to poor prognosis (Peng et al., 2020; Nissen et al., 2019), we investigated whether FMD could affect collagen remodeling and tumor stroma architecture.

In tumor sections stained with picrosirius red, collagen fiber deposition is reduced and their distribution and structure are altered in the tumor bed of the FMD group compared with the standard diet group (Figure 5A). The collagen fibers are thin and sparsely distributed, and their morphology, analyzed by polarized light, appears to be less linear and dense in the FMD group than in the standard diet group (Figure 5B).

Tumor vascular normalization enhances the efficacy of immunotherapy, as it improves tumor vessel perfusion and promotes immune effector cell infiltration in the tumor microenvironment (TME) (Zheng et al., 2018; Huang et al., 2018). To establish whether FMD in combination with immune therapy also affects tumor neovascularization, we analyzed the tumor vessels 3 days after the first cycle of FMD. FMD reduces the number of endothelial cells ($CD93^{+}$) and pericytes ($NG2^{+}$) in the tumor bed compared with the standard diet group, but the pericyte localization close to the endothelial cells is not impaired (Figure 5C). In the standard diet groups, the endothelial cells are more elongated and form a dense vascular network; instead, in the FMD group, endothelial cells look immature and poorly branched. To assess whether these FMD induced endothelium changes improve the vessels' functionality and perfusion, the tumor vessels were labeled with DyLight 488 tomato lectin, injected into the tail vein at the end of the third refeeding day after two cycles of FMD + immunotherapy treatment. In the FMD IgG group, tumors exhibit a high number of lectin-bound blood vessel structures that are less evident in the other experimental conditions (Figures S3A and S3B).

These structures do not express endothelial markers, such as CD93 and CD31, but are positive for collagen IV (Figure S3C); therefore, they may represent vascular mimicry structures generated to compensate for the lack of nutrients in FMD tumor. However, the analysis of CD93-positive tumor vessels shows that FMD reduces vessel density and tortuosity in the tumor center (Figure S3A), whereas FMD in combination with anti-OX40 affects the vascular network formation in the tumor margin, also (Figure S3B).

These results could indicate that FMD promotes immune infiltration (Figure 2F) by reducing collagen accumulation and by remodeling the tumor vascular network.

FMD preserves spleen structure and functionality, which enhances the immunotherapy response

Spleen enlargement (or splenomegaly) occurs in tumor-bearing mice (DuPre' and Hunter, 2007). Furthermore, immunotherapy-induced hyperactivation of the immune system could lead to the accumulation of exhausted T cells in the spleen.

The spleen size in FMD group was reduced compared with the standard diet group, especially in the anti-OX40 and anti-OX40/anti-PD-L1 group (Figure 1D). In the FMD group the architecture of white pulp was well preserved, showing a prominent germinal center with discrete T and B lymphocyte zones, stained with anti-B220 and anti-CD3, unlike the standard diet group, where a marked expansion of the red pulp and the myeloid population was observed (Figures S4A, S4B, and S4F). The presence of discrete follicles with active germinal centers was more notable in the FMD + anti-OX40/anti PD-L1 group than in the corresponding standard diet group.

FMD reduces extramedullary erythropoiesis and myelopoiesis, detected by anti-Ter119 and myeloperoxidase staining, and therefore could prevent the generation of myeloid cells that contribute to tumor growth through suppression of the immune system (Figures S4C–S4F).

FMD reduces the risk of anaphylaxis associated with immunotherapy

The potential of immunotherapy is limited due to high-grade adverse effects in patients (Suntharalingam et al., 2006; Lee et al., 2009; Topalian et al., 2012; Brahmer et al., 2012). In mice, repetitive doses of anti-PD1 or anti-PD-L1 in 4T1 breast cancer-bearing mice and repetitive doses of anti-OX40 in B16-F10 melanoma tumor-bearing mice cause an IgG-mediated anaphylactic shock due to the hyperactivation of neutrophils and basophils, respectively (Mall et al., 2016; Murphy et al., 2014).

Repeated single or combined treatments with anti-PD-L1 and anti-OX-40 (Figure 6A) were found to be lethal in mice fed the standard diet, but such lethality was not observed in mice also receiving FMD cycles (Figure 6B).

In particular, the fifth treatment performed on day 21 with anti-PD-L1 or anti-OX40 caused the death of 80% and 100% of the mice not receiving FMD, while 100% of the mice in the FMD group survived if treated with immunotherapy during the fasting period (Figures 6C and 6D), but not if treated during the refeeding period (data not shown). The standard diet group subjected to the double treatment showed a lethality of 20% already at the third dose of anti-PD-L1 given on day 15 of the second week,

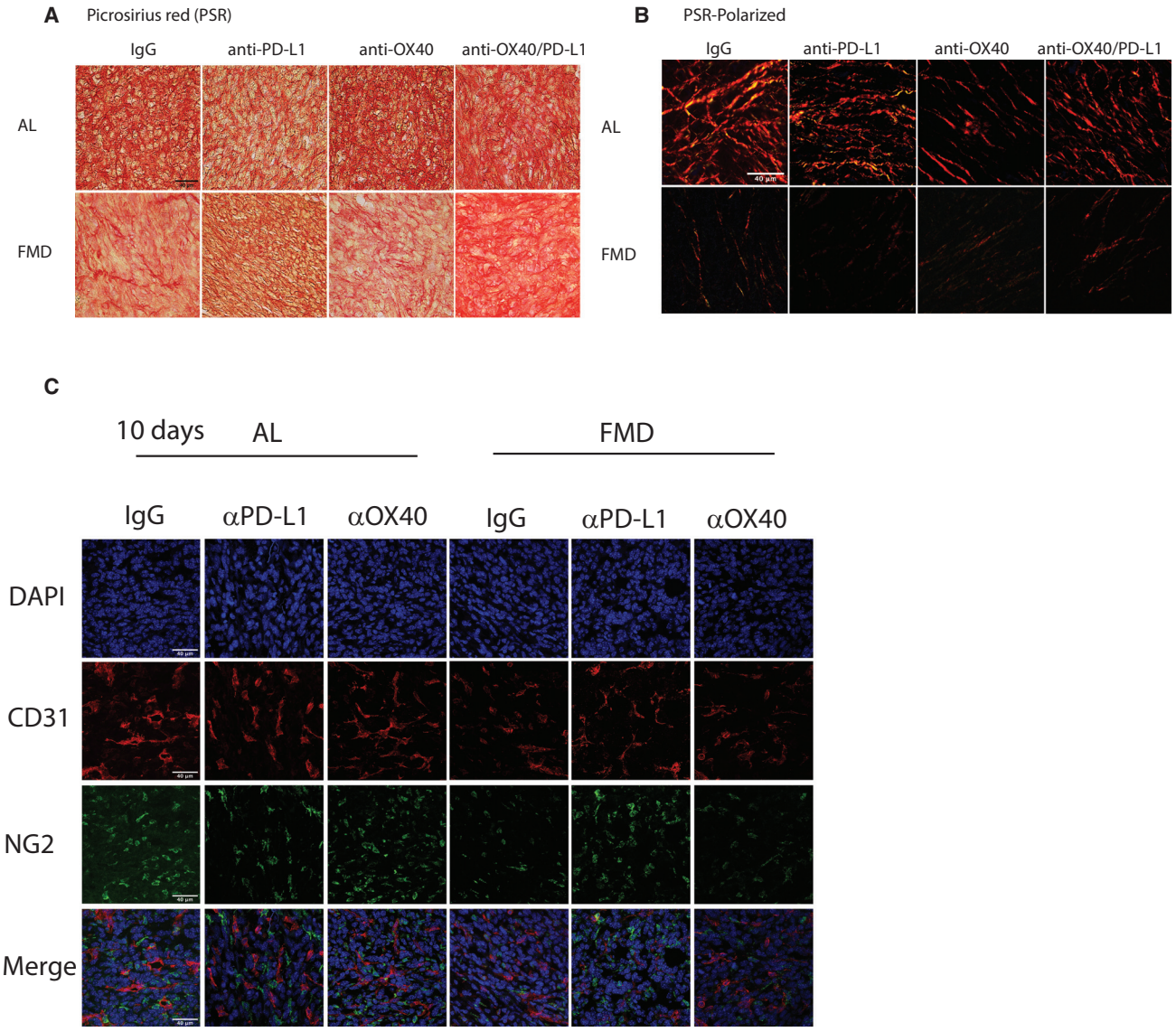

Figure 5. FMD reshapes tumor stroma and normalizes the vasculature in 4T1 breast tumor

(A–C) (A) Picrosirius red staining (PSR), (B) PSR-polarized images (scale bar, 40 μm), and (C) CD31 and NG2 dual immunostaining in 4T1, 10 days post-injection (scale bar, 40 μm).

while the lethality rose to 80% with the fourth administration of OX40 on day 21 (Figure 6E).

Succumbing mice exhibit typical symptoms of anaphylaxis within 20 min of the immune therapy injection. Since anaphylaxis depends on the activation of neutrophils and basophils and on the release of histamines, myeloperoxidase, and platelet-activating factor (PAF), we analyzed the blood of mice subjected to a standard diet or FMD with or without treatments. FMD significantly reduced the number of white blood cells, lymphocytes, monocytes, and neutrophils compared with mice fed the standard diet. Treatment with anti-OX40/anti-PD-L1 caused a major increase in the populations of eosinophils, basophils, and immature granulocytes (IGs) in the standard diet group, but not in FMD-treated mice (Figure 6F).

Furthermore, immunotherapy markedly reduced platelets and plateletcrit (PCT) in the FMD group compared with the untreated FMD group and the standard diet group with or without treatment (Figure 6F). Therefore, these FMD-induced changes in lymphocytes, monocytes, granulocytes, and platelets could prevent and attenuate the release of factors such as MPO, histamines, VEGF, and PAF that determine anaphylaxis without compromising the efficacy and duration of the therapy.

FMD enhances the efficacy of anti-OX40/anti-PD-L1 combined therapy also against a TS/A breast cancer model

Next, we explored whether FMD in combination with anti-OX40/anti-PD-L1 is also effective in the treatment of another

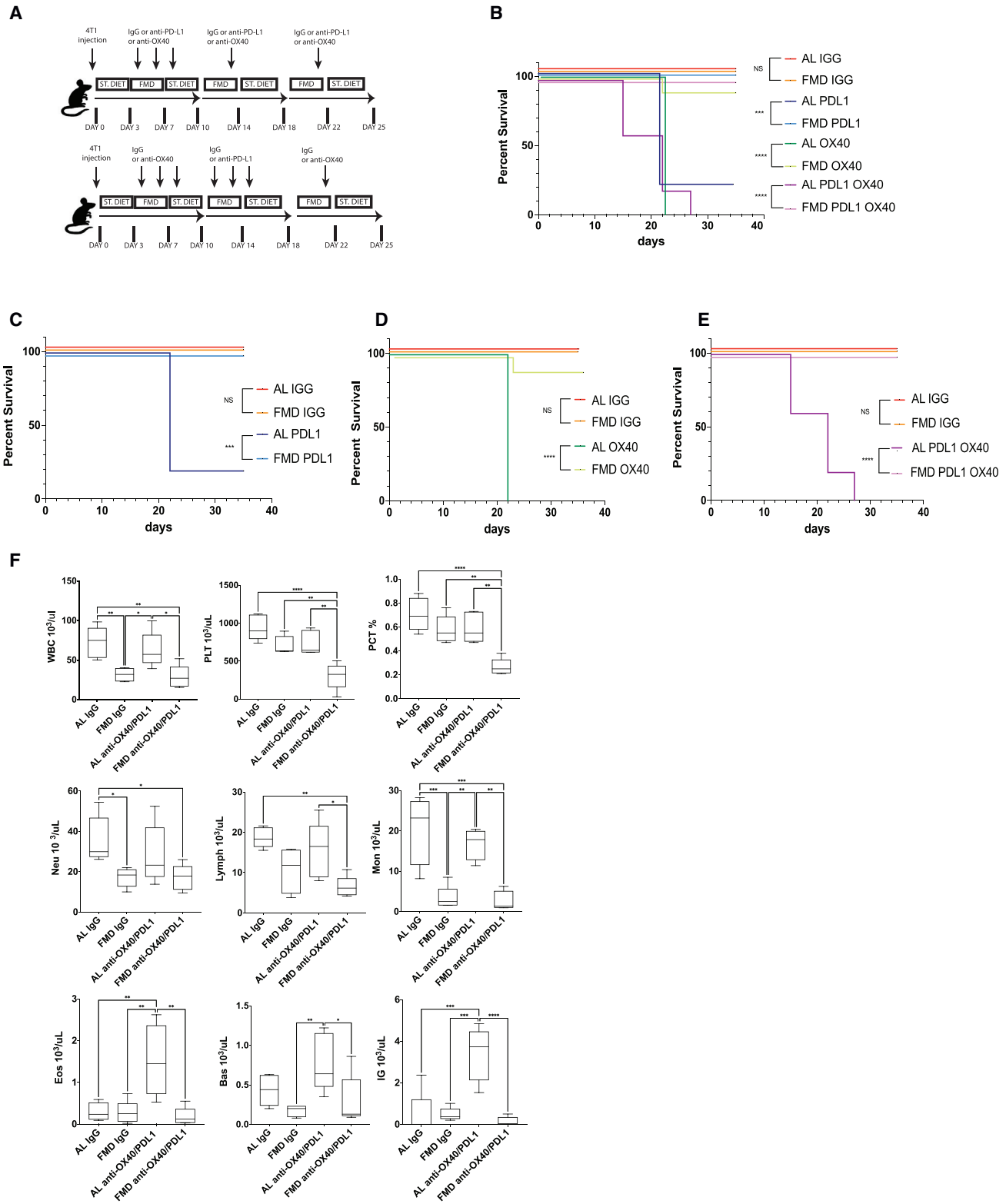

Figure 6. FMD prevents immunotherapy-related anaphylaxis in 4T1breast tumor-bearing mice

(A) Schedule of tumor implantation and treatment for 4T1 syngeneic orthotopic tumor models.

(B) Survival of BALB/c mice bearing 4T1 tumors after repeated dosing with anti-PD-L1, anti-OX40, or both (n = 10).

(legend continued on next page)

low-immunogenic mammary tumor model, TS/A (Gong et al., 2021). As observed for 4T1, FMD improves the efficacy of the anti-tumor response induced by anti-OX40/anti-PD-L1 against TS/A breast cancer compared with the standard diet and blocks tumor growth (Figure 7A), whereas FMD alone does not provide a significant anti-tumor effect in TS/A tumors. However, TS/A tumors respond better to immunotherapy alone compared with 4T1 tumor, since anti-OX40/anti-PD-L1 treatment retards tumor growth and prolongs survival (Figure S1B). Nevertheless, the effects of immunotherapy are more relevant in the FMD group than in the standard group, enabling mice in the FMD + immunotherapy group to survive for 33 days, whereas mice in the standard diet + immunotherapy group survived up to a maximum of 28 days (Figure S1B).

To determine how FMD enhances the effectiveness of the anti-OX40/anti-PD-L1 treatment, we analyzed TILs by FACS.

In breast TS/A tumors, unlike breast 4T1 tumors, FMD by itself does not increase CD3 and CD8 T cell immune infiltration (Figures S5A and S5B) and does not affect CD8 activation (Figure 7C). In this model, the treatment with anti-OX40/anti-PD-L1 expands cytotoxic and proliferating $CD8^+$ T lymphocytes ($CD8^+GzmB^+$, $CD8^+Ki67^+$) (Figure 7C), but there are no significant differences between the standard diet and the FMD. Furthermore, FMD with or without immunotherapy does not affect the infiltration and activation of $\gamma\delta$ T cells, as observed in 4T1 tumors (Figure S5C).

FMD + anti-OX40/anti-PD-L1 counteracts the reduction of conventional CD4 T cell ($FoxP3^-CD4^+$) percentage that occurs in the standard diet + immunotherapy group and promotes their activation ($OX40^+FoxP3^-CD4^+$) (Figure 7D). Interestingly, OX40 is the activation marker expressed by most conventional T cells, unlike the other two activation markers, PD1 and CD25, which are expressed by a smaller percentage of $FoxP3^-CD4^+$ T cells (Figures S5D and S5E).

FMD alone, as well as standard diet + immunotherapy, increases the percentage of immunosuppressive Treg cells ($FoxP3^+CD4^+$), whereas FMD + immunotherapy prevents this increase and maintains the same percentage of Tregs as the standard diet + IgG group (Figure 7E). However, the Tregs of the FMD group express higher levels of OX40, while the expression of PD1 and CD25 is reduced compared with the other experimental groups (Figures S5F and S5G).

Analysis of innate immune cell subsets by FACS showed an increase in the percentage of myeloid cells ($CD11b^+$) in the groups treated with immunotherapy, without finding any differences between standard diet and FMD (Figure S5H). Immunotherapy increased the percentage of NK cells ($DX5^+$) in the tumor bed, and this increase was higher in the FMD group compared with the other experimental groups (Figure 7F).

Although there are no significant differences between the various experimental groups regarding the populations of macrophages, PMN-MDSCs ($Gr1^{high}CD11b^+$), and M-MDSCs ($Ly6C^{high}CD11b^+$) (Figures S5I–S5L), FMD in combination with immunotherapy reduces the percentage of immunosuppressive M2 macrophages ($CD206^+F4/80^+CD11b^+$) but at the same time induces PD-L1 expression in PMN-MDSCs and M-MDSCs (Figures 7F, S5M, and S5N).

As observed in the 4T1 setting, also in TS/A tumors, FMD not only remodels the cellular components of the TME but also the structure and organization of the collagen fibers in the tumor bed (Figure 7G). In the FMD group, the density and thickness of collagen fibers is lower than in the standard diet groups.

FMD reverses TME immunosuppression by reducing the immunosuppressive myeloid cell population

To establish how FMD affects TME, we analyzed tumor immune infiltrate in 4T1 and TS/A tumor masses collected at the end of the second cycle of FMD (Figure S6A). FMD significantly reduces the growth of 4T1 tumors but not TS/A tumors (Figure S6B); induces a significant reduction in the myeloid immunosuppressive population (CD11b), immunosuppressive M2 macrophages (CD206/F4/80), PMN-MDSC ($Gr1^{high}$), and M-MDSC ($Ly6C^{high}$) population; and reduces PD-L1 expression on both polymorfonuclear (PMN) MDSCs and monocytic (M) MDSCs in 4T1 tumors (Figure S6C). In TS/A tumors, on the other hand, only the M-MDSC population undergoes a significant reduction upon two cycles of FMD (Figure S6C), whereas the other immunosuppressive myeloid populations do not change in the FMD group compared with the control (AL) (Figure S6C).

There is no significant variation in the population of ($Foxp3^+CD4$) Tregs between the standard group (AL) and the FMD group (Figure S7A) in 4T1 tumors; however, the expression of Treg activation markers, such as CTLA4 and PD1, is higher in the FMD group than in the standard group.

In TS/A tumors, FMD does not have an impact on the Treg population ($FoxP3^+CD4$); however, it significantly increases the expression of OX40 and PD1 (Figure S7B). It is plausible that such high expression of OX40 and PD1 in the FMD group could render Treg cells more sensitive to anti-OX40/anti-PD-L1 therapy and thus prevent the increase of this population in the FMD + immunotherapy group (Figure 7E).

FMD enhances immunotherapy efficacy by reactivating early dysfunctional effector T cells

Immunotherapy generates a durable anti-tumoral immune response by reactivating early exhausted effector T cells that already existed pretherapy (Miller et al., 2019; Siddiqui et al., 2019; Kurtulus et al., 2019). The early exhausted effector T cells differ from the late exhausted effector T cell subpopulation because: (1) they are tumor reactive, (2) they restore cytokine production and cytotoxicity upon immunotherapy treatment, and (3) they express a high level of TCF7 and low levels of TIM3 (*Havcr2*), PD1 (*Pdcd1*), LAG3, and CD39 (*Entpd1*)

(C–E) Survival of BALB/c mice after repeated doses of (C) anti-PD-L1, (D) anti-OX40, and (E) anti-OX40/anti-PD-L1.
(F) White blood cell (WBC), platelet (PLT), plateletcrit (PCT), neutrophil (Neu), lymphocyte (Lymph), monocyte (Mon), eosinophil (Eos), basophil (Bas), and immature granulocyte (IG) counts from mice fed with standard diet or FMD and treated with IgG or anti-OX40/anti-PD-L1, assessed with an AcT5 Diff. hematology analyzer (n = 5). Survival analysis was plotted according to the Kaplan-Meier method, and statistical differences were determined with the log-rank test. The p values from two-way ANOVA were *$p < 0.05$, **$p < 0.005$, ***$p < 0.0005$, and ****$p < 0.0001$.

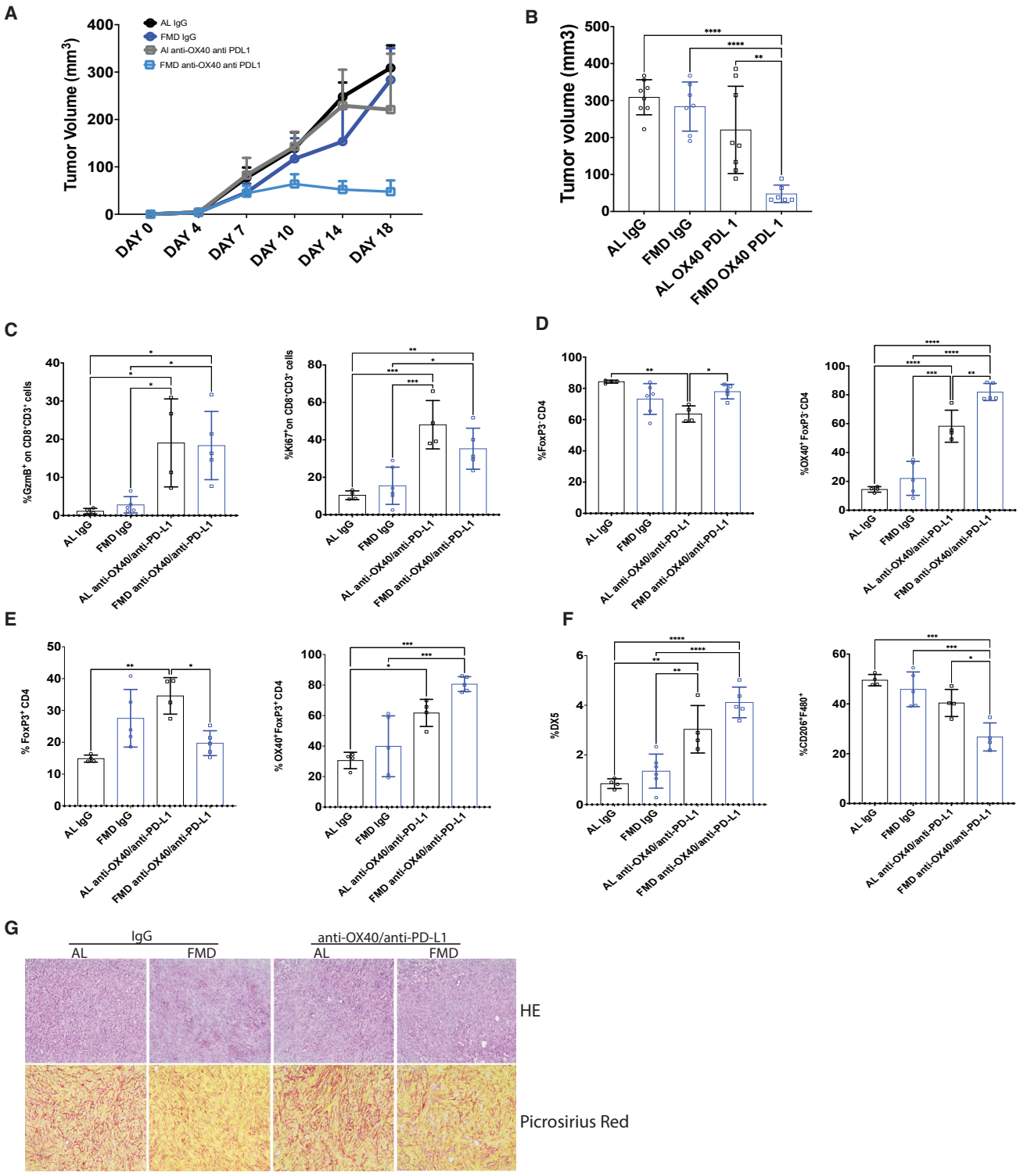

Figure 7. FMD with anti-OX40/anti-PD-L1 therapy is effective in delaying TS/A tumor growth by modulating CD4 T cell activity and reducing immunosuppressive M2 macrophages

(A and B) TS/A tumor growth in immunocompetent BALB/c syngeneic mice treated with isotype control and anti-OX40/anti-PD-L1 and fed with standard diet or FMD (n = 8).

(legend continued on next page)

(Sade-Feldman et al., 2018; Fehlings et al., 2017; Gubin et al., 2018).

scRNA and FACS analyses were performed on tumor immune infiltrates to determine whether FMD improved immunotherapy efficacy by modulating the early exhausted effector T cells to late exhausted effector T cells transition.

To better characterize the heterogeneity at the level of the *Cd8*$^+$ T cell compartment, we performed unsupervised clustering analysis on CD8$^+$ cells belonging to the T cell macrogroup. We identified five *Cd8*$^+$ subclusters with specific gene signatures: clusters 4 and 5 (T memory stem cells) express *Tcf7*, *Sell*, and *Ly6c1*; cluster 3 (effector T cells) expresses *GzmB*, *GzmK*, and a low level of *Havcr2*; cluster 2 (late dysfunctional effector T cells) expresses inhibitory receptor genes (*Pdcd1*, *Lag3*, *Tnfrsf9*) and an exhaustion-specific transcription factor, *Tox*; cluster 1 (early exhausted effector T cells) expresses *Tcf7* and low levels of inhibitor receptor genes (*Pdcd1*, *Lag3*, *Tnfrsf9*, and *Tox*); and cluster 0 (exhausted T cells) expresses *Tox* and intermediate-high levels of inhibitory receptors (*Pdcd1*, *Lag3*, *Tnfrsf9*) (Figure S8A). The clusters are arranged within a UMAP projection outlining a top-down trajectory associated with the differentiation state of the T cells that pass from an undifferentiated stem state (clusters 4–5, *Tcf7* high expression) at the top, to an early state of differentiation and activation (clusters 1–3) (*Tcf7* high expression, *Tox* low expression), to end up in a highly differentiated and exhausted state represented by clusters 0–2 at the bottom (Tox high expression) (Figure S8A).

The cluster cell proportion, estimated from scRNA analysis, shows that the early exhausted effector T cell population is enriched more in the FMD groups independent of immunotherapy, relative to the corresponding standard diet groups (Figure S8A).

Notably, late exhausted effector T cells increased in the FMD untreated group compared with the standard diet group, while immunotherapy reduced the percentage of late exhausted T cells in both the standard diet and the FMD groups (Figure S8A).

FACS analysis showed also that FMD and anti-OX40/anti-PD-L1 treatment increases the TIM3$^+$ and TIM3$^+$PD1$^+$ CD8 exhausted T cell population compared with the standard diet control group (Figure S8B). However, the increase in exhausted T cells is correlated with a greater activation of T cells (PD1$^+$Ki67$^+$CD8) induced by both FMD and immunotherapy compared with the untreated standard diet group. Indeed, the active PD1$^+$Ki67$^+$CD8 population increases significantly in the FMD group and in immunotherapy groups compared with the untreated standard diet group (Figure S8B).

We then determined whether FMD and immunotherapy affect the early and late exhausted effector T cells, characterized by low or intermediate expression of PD1, TOX, and CD39 (CD39^{low}PD1^{int}TOX^{int}CD8), unlike late exhausted effector T cells, which express high levels of TOX, PD1, and CD39 (CD39^{high}PD1^{high}TOX^{high}CD8). FACS analysis of 4T1 immune infiltrates showed that FMD and immunotherapy increases PD1^{int}TOX^{int}CD8 exhausted effector T cells (Figure S8C), whereas FMD in combination with anti-OX40/anti-PD-L1 induces a significant increase in CD39^{low}PD1^{int}TOX^{int}CD8 early exhausted effector T cells (Figure S8C), which could be reprogrammed and reactivated by immunotherapy.

To assay CD8 T cell activation and cytotoxicity, cell suspensions from 4T1 tumor masses were treated *ex vivo* with phorbol myristate acetate (PMA), ionomycin, and brefeldin A for 2 h and analyzed for the expression of markers such as PD1, Ki67, and IFNγ.

FMD, as well as immunotherapy, increases the proliferating Ki67$^+$CD8 T and Ki67$^+$PD1$^+$CD8 T cell population, whereas FMD with or without immunotherapy induces a higher IFNγ production in CD8 T cells (IFNγ^+CD8) than the untreated or treated standard diet group (Figure S8D).

FACS analysis performed on TS/A tumor immune infiltrate confirmed that FMD and immunotherapy increases the proliferating and active Ki67$^+$PD1$^+$CD8 T cells but also the exhausted TIM3$^+$PD1$^+$CD8 T cells (Figure S9A). FMD has a mild effect on the TOX^{int}PD1^{int}CD8 exhausted T cell population, whereas immunotherapy increases this cell population, even if not significantly (Figure S9B). However, FMD in combination with anti-OX40/anti-PD-L1 significantly increases TOX^{int}PD1^{int}CD39^{low}CD8 early exhausted effector T cells, thus favoring CD8 T cell activation and improving the anti-tumor immune response (Figure S9B). FMD with or without immunotherapy promotes the IFNγ production in CD8 T cells (IFNγ^+CD8) stimulated *in vitro* (Figure S9C), as previously observed in 4T1 immune-infiltrates.

These data demonstrate that FMD improves the anti-tumor efficacy of immunotherapy by reprogramming the population of early exhausted effector CD8 T cells, thus promoting their reactivation and the release of cytokines such as IFNγ.

FMD promotes metabolic shift from glycolysis to oxidative phosphorylation (OXPHOS)

We next examined whether FMD can affect cellular metabolism, lactic acid production, and the pH in the TME. To this end, we performed an untargeted metabolomic analysis on 4T1 and TS/A tumors collected on the last day of FMD.

Partial least squares-discriminate analysis (PLS-DA) and a hierarchical clustering heatmap clearly discriminate two clusters between FMD and standard diet in 4T1 and TS/A tumors (Figures S10A and S10B) and between 4T1 and TS/A tumors belonging to the standard diet group (Figure S10C).

In 4T1 tumors, the Small Molecule Pathway Database (SMPDB) pathways enrichment analysis showed that FMD affects pathways involved in ketone body metabolism, carnitine synthesis, fatty acid oxidation, and mitochondrial electron transport chain compared with the standard diet group.

FMD significantly increases the levels of carnitine, pantothenic acid, and docosahexaenoic acid, while reducing the levels of acetylcarnitine (Figure S10A). There is an upward trend of the lipid profile, such as oleic, palmitic, arachidonic, and linolenic

(C–F) Frequency of tumor (C) GzmB$^+$CD8$^+$CD3$^+$ and Ki67$^+$CD8$^+$CD3$^+$ T lymphocytes, (D) FoxP3$^-$CD4$^+$CD3$^+$ and OX40$^+$FoxP3$^-$CD3$^+$CD4$^+$ conventional T cells, (E) FoxP3$^+$CD4$^+$CD3$^+$ and OX40$^+$FoxP3$^+$CD4$^+$CD3$^+$ regulatory T cells, and (F) DX5T NK cells and CD206$^+$F4/80$^+$Cd11b$^+$ M2 macrophages (n = 5).
(G) TS/A tumor sections stained with hematoxylin and eosin (HE) or picrosirius red. The p values from two-way ANOVA were *p < 0.05, **p < 0.005, ***p < 0.0005, and ****p < 0.0001.

acid, confirmed by immunohistochemical analysis of 4T1 tumor sections, stained with oil red (Figure S10D), and of *cis*-aconitic acid (citrate intermediate) levels in the FMD group compared with the standard diet. No significant differences were detected in glycolysis metabolites such as glucose and pyruvate, whereas the lactic acid level is lowered in FMD 4T1 tumors (Figure S10A). These data could imply that FMD promotes the pyruvic acid conversion to acetyl-CoA instead of lactic acid. Since carnitine mediates the transport of fatty acids to the mitochondrion, where β-oxidation takes place, pantothenic acid is mainly involved in the synthesis of CoA, and fasting increases the expression of carnitine palmitoyltransferase (CPT), the rate-limiting enzyme of β-oxidation, in rat tissues (Luci et al., 2008), FMD should promote citrate cycle activity through the β-oxidation of fatty acids and the formation of acetyl-CoA.

In TS/A tumors, FMD increases the level and catabolism of amino acids such as alanine, glycine, and methionine (Figure S10B); the urea cycle activity (ornithine, citrulline, and urea level); and the synthesis of intracellular energy reserve compounds such as creatine-phosphocreatine (Figure S10B). Glucose, pyruvate, and lactic acid (glycolysis intermediates) levels are significantly reduced in the FMD group compared with the standard diet (Figure S10B). There are no significant differences in carnitine and fatty acid (oleic acid and docosahexaenoic acid) levels between the FMD and the standard diet group, although the pantothenic acid level is higher in FMD tumors than in the standard diet group. However, lipid droplets accumulate in the standard diet group, whereas they decrease in the FMD group in TS/A tumor sections stained with oil red (Figure S10D).

The comparison of 4T1 and TS/A tumor metabolic profiles from the standard diet groups reveals that the levels of carnitine, fatty acids (oleic acid, docosahexaenoic acid), pantothenic acid, and *cis*-aconitic acid are much higher in TS/A tumors than in 4T1 tumors; therefore, the TS/A tumor metabolism relies on fatty acid β-oxidation and on oxidative phosphorylation (Gong et al., 2021), unlike 4T1 tumors, whose metabolism depends on glycolysis, given the high levels of glucose-6p and fructose-6p (glycolysis intermediates) (Figure S10C).

It is possible that FMD increases fatty acid β-oxidation and citrate cycle activity in TS/A tumors, as evidenced by the reduction of fatty acid droplets (Figure S10D), whereas it leads to a metabolic shift from glycolysis to oxidative phosphorylation in 4T1 tumors, which could contribute to slowing 4T1 tumor growth.

DISCUSSION

In this study we show that combination FMD with anti-OX40/anti-PD-L1 therapy enhances the anti-tumor immune response against two different low-immunogenic triple-negative breast cancer (TNBC) subtypes (4T1 and TS/A). Immunotherapy has a strong effect in retarding tumor growth when combined with FMD cycles, an effect not observed in combination with the standard diet. Notably, the anti-tumor immune response induced by immunotherapy and FMD is positive but different in 4T1 and TS/A breast cancers, consistent with our hypothesis that fasting/FMD conditions are effective not by promoting specific mechanisms conserved in many tumor cell types but by generating differential stress sensitization (DSS) conditions that sensitize the great majority of cancer cells, but not normal cells, to toxic environments.

In both 4T1 and TS/A tumors, FMD improves the efficacy of immunotherapy by modulating the population of early exhausted effector T cells, which can be reactivated by immunotherapy and exert the anti-tumor response.

Fasting/FMD cycles reduce the circulating levels of IGF-1 but also mTOR signaling in normal cells. Transient inhibition of mTOR *ex vivo* and *in vivo* can lead to early exhausted effector T cell expansion as well as improved response to immune checkpoint blockade in chronic viral infection (Gabriel et al., 2021). Early exhausted effector T cells display higher mitochondrial mass and better mitochondrial fitness compared with late exhausted effector T cells. These mitochondrial changes are associated with high OXPHOS capacity, essential for supporting the early exhausted effector T cells' self-renewal (Gabriel et al., 2021). Fasting also shifts the TME metabolism from glycolysis to OXPHOS, since we observed evidence for increased β-oxidation of fatty acids. Such fasting-induced metabolic changes in the TME could promote the selective expansion of early exhausted effector T cells at the expense of late exhausted effector T cells whose metabolism is poorly suited to these physiological conditions.

The increase in OXPHOS activity and the scarcity of nutrients could also lead to a cytoplasmic reduction of key metabolic intermediates of the Krebs cycle, such as acetyl-CoA, and of methionine, both involved in epigenetic modifications. One possibility is that FMD could promote the expansion of early exhausted effector T cells through metabolite-regulated epigenetic remodeling (Vodnala et al., 2019; Collins et al., 2019; Longo et al., 2020), thus improving the anti-tumor immune response of the immune checkpoint blockade.

The high ketone bodies level and the inhibition of mTOR caused by FMD cycles could also favor the accumulation and activation of γδ T cells in breast tissue and strengthen the anti-tumor immune response of cytotoxic CD8 T cells. γδ T cells, particularly the Vδ1$^+$ subtype, can orchestrate an effective anti-tumor response as supported by the positive correlation of their presence with better prognosis in TNBC patients (Silva-Santos et al., 2019). Notably, ketone bodies produced by a ketogenic diet have been shown to promote the expansion and activation of γδ T cells in the visceral mass (Goldberg et al., 2020), while the mTOR inhibition impairs the development of αβ T cells but promotes γδ T cell generation in the thymus (Yang et al., 2018) (Figure S11).

These changes exerted by FMD on the immune infiltrate in the 4T1 TME are also associated with a remodeling of the tumor vessels and the extracellular matrix. FMD could improve vessel functionality and perfusion and reduce the deposition of collagen in the TME by mTOR inhibition. In fact, targeted mTOR inhibition suppresses the release of collagen by fibroblasts (Hettiarachchi et al., 2020), decreases the tumor vascular meshwork in a variety of solid tumor models (Lane et al., 2009; Du et al., 2013), and improves the efficacy of immunotherapy (Lastwika et al., 2016).

In the breast 4T1 model, FMD reduces the risk of anaphylaxis associated with immunotherapy by reducing the number of lymphocytic, monocytic, and granulocytic populations, whose activation can trigger anaphylactic shock. Notably, the lethality

associated with such immunotherapies in mice is specific and is mainly observed in certain mouse cancer models but could reflect the toxicity of immunotherapy in at least a portion of the patient population.

The TS/A TNBC tumor is also very sensitive to the combination of FMD plus immunotherapy, but the mechanisms responsible for this effect are partly distinct from those observed with 4T1 cells. The anti-tumor response induced by FMD + immunotherapy against this subtype of breast tumor is mainly mediated by the activation of conventional T cells, expansion of early exhausted effector T cells, and reduction of the percentage of immunosuppressive Treg cells. In addition, FMD modulates the innate immune compartment, by promoting the infiltration of NK cells and reducing immune-suppressive M2 polarized macrophages and the collagen deposition in the TME. Unlike what was observed for the 4T1 model, FMD does not act on the recruitment and activation of CD8 and $\gamma\delta$ T cells and does not lead to the depletion of the immunosuppressive PMN-MDSCs in the TS/A TME. Lipogenic TS/A tumors show a much lower percentage of myeloid infiltrate compared with glycolytic 4T1 tumors (40% versus 70%), which could affect the modulation of the immune response and the shaping of the same microenvironment (Figure S11).

In summary, in this study we show that FMD switches the metabolism from glycolysis to oxidative phosphorylation, reshapes the TME, and enhances the efficacy of immunotherapy in two different TNBC tumor types, possibly by increasing the early exhausted effector T cells. Thus, FMD cycles may represent a promising nutritional intervention and should continue to be tested clinically for their effects in sensitizing low-immunogenic tumors to immunotherapy to improve the portion of cancer types and patients responsive to the treatment.

Limitations of the study

Because metabolic and physiological changes in mice are much more dramatic than in humans, the beneficial effects of FMD on TME and the immune system may not occur in humans or could be smaller. However, the initial clinical trials in oncology patients recapitulate the physiological, hormonal, and immune system changes observed in preclinical studies, making FMD cycles a promising intervention to enhance immunotherapy.

STAR★METHODS

Detailed methods are provided in the online version of this paper and include the following:

- KEY RESOURCES TABLE
- RESOURCE AVAILABILITY
  - Lead contact
  - Materials availability
  - Data and code availability
- EXPERIMENTAL MODEL AND SUBJECT DETAILS
  - Tumor cell lines
  - Mice
- METHOD DETAILS
  - Tumor implantation, immune checkpoint blockade (ICB) treatment, and tumor volume measurement
  - Flow cytometry analysis of tumor-infiltrating lymphocytes and apoptosis
  - Complete blood counts
  - Immunohistochemistry
  - Preparation of single-cell suspension
  - Droplet-based single-cell sequencing
  - Vascular perfusion
  - Sample preparation for metabolomic analysis
- QUANTIFICATION AND STATISTICAL ANALYSIS
  - ScRNA data pre-processing and clustering
  - Cell type annotation and cluster name assignation
  - Subclustering
  - Differential expression gene analysis
  - Metabolomic data analysis
  - Morphometric analysis

SUPPLEMENTAL INFORMATION

Supplemental information can be found online at https://doi.org/10.1016/j.celrep.2022.111256.

ACKNOWLEDGMENTS

We thank the IFOM Imaging and Histopathology Facility, Cogentech Microarray Facility, and IEO Genomic Unit for technical support. This work was supported by the Associazione Italiana per la Ricerca sul Cancro (AIRC; IG#17605 and IG#21820 to V.D.L. and IG#20109 to A.R. and F.B.; Italian Ministry of Health [Ricerca Corrente] to A.R. and F.B.). The authors would like to thank Laura Carpen, Giulia Graziano, and Francesco Ferrari for insightful comments regarding scRNA-seq analyses and results, and the IFOM/IEO Genomic Unit, in particular Luca Rotta, Mirco Riboni, Claudia Valli, and Simone Minardi, for scRNA-seq library preparation.

AUTHOR CONTRIBUTIONS

S.C., E.V., V.S., G.F., and F.F. performed all the *in vivo* and *in vitro* experiments. C.C. and G.D. carried out FACS analysis. F.P. performed IHC analysis. S.M. helped to design an ImaJ plug-in for blood vessel analysis. A.R. and S.C. designed and performed the computational analyses for scRNA-sequencing data, supervised by F.B. F.I. and F.Z. participated in scRNA-sequencing analysis. G.C., P.D., M.P.C., and C.T. provided expertise and feedback. All authors discussed the results and contributed to the final manuscript. S.C. and V.D.L. conceived and designed the study and drafted the manuscript.

DECLARATION OF INTERESTS

V.D.L. holds intellectual property rights on clinical uses of FMD and equity interest in L-Nutra, a company that markets medical food.

Received: October 25, 2021
Revised: May 10, 2022
Accepted: July 28, 2022
Published: August 23, 2022

REFERENCES

Ajona, D., Ortiz-Espinosa, S., Lozano, T., Exposito, F., Calvo, A., Valencia, K., Redrado, M., Remírez, A., Lecanda, F., Alignani, D., et al. (2020). Short-term starvation reduces IGF-1 levels to sensitize lung tumors to PD-1 immune checkpoint blockade. Nat. Cancer *1*, 75–85.

Aran, D., Looney, A.P., Liu, L., Wu, E., Fong, V., Hsu, A., Chak, S., Naikawadi, R.P., Wolters, P.J., Abate, A.R., et al. (2019). Reference-based analysis of lung single- cell sequencing reveals a transitional profibrotic macrophage. Nat. Immunol. *20*, 163–172.

Bayne, L.J., Beatty, G.L., Jhala, N., Clark, C.E., Rhim, A.D., Stanger, B.Z., and Vonderheide, R.H. (2012). Tumor-derived granulocyte-macrophage colony-stimulating factor regulates myeloid inflammation and T cell immunity in pancreatic cancer. Cancer Cell *21*, 822–835.

Blighe, K., Rana, S., and Lewis, M. (2021). EnhancedVolcano: publication-ready volcano plots with enhanced colouring and labeling. R package version 1.10.0. https://github.com/kevinblighe/EnhancedVolcano.

Brahmer, J.R., Tykodi, S.S., Chow, L.Q.M., Hwu, W.J., Topalian, S.L., Hwu, P., Drake, C.G., Camacho, L.H., Kauh, J., Odunsi, K., et al. (2012). Safety and activity of anti-PD-L1 antibody in patients with advanced cancer. N. Engl. J. Med. *366*, 2455–2465.

Brandhorst, S., Choi, I.Y., Wei, M., Cheng, C.W., Sedrakyan, S., Navarrete, G., Dubeau, L., Yap, L.P., Park, R., Vinciguerra, M., et al. (2015). A periodic diet that mimics fasting promotes multi-system regeneration, enhanced cognitive performance, and healthspan. Cell Metab. *22*, 86–99.

Caffa, I., Spagnolo, V., Vernieri, C., Valdemarin, F., Becherini, P., Wei, M., Brandhorst, S., Zucal, C., Driehuis, E., Ferrando, L., et al. (2020). Fasting-mimicking diet and hormone therapy induce breast cancer regression. Nature *583*, 620–624.

Cheng, C.W., Adams, G.B., Perin, L., Wei, M., Zhou, X., Lam, B.S., Da Sacco, S., Mirisola, M., Quinn, D.I., Dorff, T.B., et al. (2014). Prolonged fasting reduces IGF-1/PKA to promote hematopoietic-stem-cell-based regeneration and reverse immunosuppression. Cell Stem Cell *14*, 810–823.

Collins, N., Han, S.J., Enamorado, M., Link, V.M., Huang, B., Moseman, E.A., Kishton, R.J., Shannon, J.P., Dixit, D., Schwab, S.R., et al. (2019). The bone marrow protects and optimizes immunological memory during dietary restriction. Cell *178*, 1088–1101.e15.

de Groot, S., Lugtenberg, R.T., Cohen, D., Welters, M.J.P., Ehsan, I., Vreeswijk, M.P.G., Smit, V.T.H.B.M., de Graaf, H., Heijns, J.B., Portielje, J.E.A., et al.; Dutch Breast Cancer Research Group BOOG (2020). Fasting mimicking diet as an adjunct to neoadjuvant chemotherapy for breast cancer in the multicentre randomized phase 2 DIRECT trial. Nat. Commun. *11*, 3083.

Di Biase, S., Lee, C., Brandhorst, S., Manes, B., Buono, R., Cheng, C.W., Cacciottolo, M., Martin-Montalvo, A., de Cabo, R., Wei, M., et al. (2016). Fasting-mimicking diet reduces HO-1 to promote T cell-mediated tumor cytotoxicity. Cancer Cell *30*, 136–146.

Du, W., Gerald, D., Perruzzi, C.A., Rodriguez-Waitkus, P., Enayati, L., Krishnan, B., Edmonds, J., Hochman, M.L., Lev, D.C., and Phung, T.L. (2013). Vascular tumors have increased p70 S6-kinase activation and are inhibited by topical rapamycin. Lab. Invest. *93*, 1115–1127.

DuPre', S.A., and Hunter, K.W., Jr. (2007). Murine mammary carcinoma 4T1 induces a leukemoid reactionwith splenomegaly: association with tumor-derived growth factors. Exp. Mol. Pathol. *82*, 12–24.

Fehlings, M., Simoni, Y., Penny, H.L., Becht, E., Loh, C.Y., Gubin, M.M., Ward, J.P., Wong, S.C., Schreiber, R.D., and Newell, E.W. (2017). Checkpoint blockade immunotherapy reshapes the high-dimensional phenotypic heterogeneity of murine intratumoural neoantigen-specific CD8 + T cells. Nat. Commun. *8*, 562.

Flynn, S., Toellner, K.M., Raykundalia, C., Goodall, M., and Lane, P. (1998). CD4 T cell cytokine differentiation: the B cell molecule, OX-40 ligand, instructs CD4 T cells to express IL-4 and upregulates expression of the chemokine receptor, Blr-1. J. Exp. Med. *188*, 297–304.

Gabriel, S.S., Tsui, C., Chisanga, D., Weber, F., Llano-León, M., Gubser, P.M., Bartholin, L., Souza-Fonseca-Guimaraes, F., Huntington, N.D., Shi, W., et al. (2021). Transforming growth factor-β-regulated mTOR activity preserves cellular metabolism to maintain long-term T cell responses in chronic infection. Immunity *54*, 1698–1714.e5.

Germain, P.L., Sonrel, A., and Robinson, M.D. (2020). pipeComp, a general framework for the evaluation of computational pipelines, reveals performant single cell RNA-seq preprocessing tools. Genome Biol. *21*, 227.

Germain, P. (2021). scDblFinder: scDblFinder. R package version 1.6.0. https://github.com/plger/scDblFinder.

Goldberg, E.L., Shchukina, I., Asher, J.L., Sidorov, S., Artyomov, M.N., and Dixit, V.D. (2020). Ketogenesis activates metabolically protective γδ T cells in visceral adipose tissue. Nat. Metab. *2*, 50–61.

Gong, Y., Ji, P., Yang, Y.S., Xie, S., Yu, T.J., Xiao, Y., Jin, M.L., Ma, D., Guo, L.W., Pei, Y.C., et al. (2021). Metabolic-pathway-based subtyping of triple-negative breast cancer reveals potential therapeutic targets. Cell Metab. *33*, 51–64.e9.

Gough, M.J., Ruby, C.E., Redmond, W.L., Dhungel, B., Brown, A., and Weinberg, A.D. (2008). OX40 agonist therapy enhances CD8 infiltration and decreases immune suppression in the tumor. Cancer Res. *68*, 5206–5215.

Gu, Z., Eils, R., and Schlesner, M. (2016). Complex heatmaps reveal patterns and correlations in multidimensional genomic data. Bioinformatics *32*, 2847–2849.

Gubin, M.M., Esaulova, E., Ward, J.P., Malkova, O.N., Runci, D., Wong, P., Noguchi, T., Arthur, C.D., Meng, W., Alspach, E., et al. (2018). High-dimensional analysis delineates myeloid and lymphoid compartment remodeling during successful immune-checkpoint cancer therapy. Cell *175*, 1030–1443.

Heng, T.S.P., and Painter, M.W.; Immunological Genome Project Consortium (2008). The Immunological Genome Project: networks of gene expression in immune cells. Nat. Immunol. *9*, 1091–1094.

Herbst, R.S., Soria, J.C., Kowanetz, M., Fine, G.D., Hamid, O., Gordon, M.S., Sosman, J.A., McDermott, D.F., Powderly, J.D., Gettinger, S.N., et al. (2014). Predictive correlates of response to the anti-PD-L1 antibody MPDL3280A in cancer patients. Nature *515*, 563–567.

Hettiarachchi, S.U., Li, Y.H., Roy, J., Zhang, F., Puchulu-Campanella, E., Lindeman, S.D., Srinivasarao, M., Tsoyi, K., Liang, X., Ayaub, E.A., et al. (2020). Targeted inhibition of PI3 kinase/mTOR specifically in fibrotic lung fibroblasts suppresses pulmonary fibrosis in experimental models. Sci. Transl. Med. *12*, eaay3724.

Huang, Y., Kim, B.Y.S., Chan, C.K., Hahn, S.M., Weissman, I.L., and Jiang, W. (2018). Improving immune-vascular crosstalk for cancer immunotherapy. Nat. Rev. Immunol. *18*, 195–203.

Imura, A., Hori, T., Imada, K., Ishikawa, T., Tanaka, Y., Maeda, M., Imamura, S., and Uchiyama, T. (1996). The human OX-40/gp34 system directly mediates adhesion of activated T cells to vascular endothelial cells. J. Exp. Med. *183*, 2185–2195.

Johnsson, K., Soneson, C., and Fontes, M. (2015). Low bias local intrinsic dimension estimation from expected simplex skewness. IEEE Trans. Pattern Anal. Mach. Intell. *37*, 196–202.

Kim, K., Skora, A.D., Li, Z., Liu, Q., Tam, A.J., Blosser, R.L., Diaz, L.A., Jr., Papadopoulos, N., Kinzler, K.W., Vogelstein, B., and Zhou, S. (2014). Eradication of metastatic mouse cancers resistant to immune checkpoint blockade by suppression of myeloid-derived cells. Proc. Natl. Acad. Sci. USA *111*, 11774–11779.

Kjaergaard, J., Tanaka, J., Kim, J.A., Rothchild, K., Weinberg, A., and Shu, S. (2000). Therapeutic efficacy of OX-40receptor antibody depends on tumor immunogenicity and anatomic site of tumor growth. Cancer Res. *60*, 5514–5521.

Krishnamoorthy, M., Gerhardt, L., and Maleki Vareki, S. (2021). Immunosuppressive effects of myeloid-derived suppressor cells in cancer and immunotherapy. Cells *10*, 1170.

Kurtulus, S., Madi, A., Escobar, G., Klapholz, M., Nyman, J., Christian, E., Pawlak, M., Dionne, D., Xia, J., Rozenblatt-Rosen, O., et al. (2019). Checkpoint blockade immunotherapy induces dynamic changes in PD-1 - CD8 + tumor-infiltrating T cells. Immunity *50*, 181–194.e6.

Lane, H.A., Wood, J.M., McSheehy, P.M.J., Allegrini, P.R., Boulay, A., Brueggen, J., Littlewood-Evans, A., Maira, S.M., Martiny-Baron, G., Schnell, C.R., et al. (2009). mTOR inhibitor RAD001 (everolimus) has antiangiogenic/vascular properties distinct from a VEGFR tyrosine kinase inhibitor. Clin. Cancer Res. *15*, 1612–1622.

Lastwika, K.J., Wilson, W., 3rd, Li, Q.K., Norris, J., Xu, H., Ghazarian, S.R., Kitagawa, H., Kawabata, S., Taube, J.M., Yao, S., et al. (2016). Control of PD-L1

expression by oncogenic activation of the AKT-mTOR pathway in non-small cell lung cancer. Cancer Res. *76*, 227–238.

Lee, C., Raffaghello, L., Brandhorst, S., Safdie, F.M., Bianchi, G., Martin-Montalvo, A., Pistoia, V., Wei, M., Hwang, S., Merlino, A., et al. (2012). Fasting cycles retard growth of tumors and sensitize a range of cancer cell types to chemotherapy. Sci. Transl. Med. *4*, 124ra27.

Lee, S.W., Salek-Ardakani, S., Mittler, R.S., and Croft, M. (2009). Hypercostimulation through 4-1BB distorts homeostasis of immune cells. J. Immunol. *182*, 6753–6762.

Longo, V.D., and Cortellino, S. (2020). Fasting, dietary restriction, and immunosenescence. J. Allergy Clin. Immunol. *146*, 1002–1004.

Luci, S., Hirche, F., and Eder, K. (2008). Fasting and caloric restriction increases mRNA concentrations of novel organic cation transporter-2 and carnitine concentrations in rat tissues. Ann. Nutr. Metab. *52*, 58–67.

Mölder, F., Jablonski, K.P., Letcher, B., Hall, M.B., Tomkins-Tinch, C.H., Sochat, V., Forster, J., Lee, S., Twardziok, S.O., Kanitz, A., et al. (2021). Sustainable data analysis with Snakemake. F1000Res. *10*, 33.

Ma, Y., Li, J., Wang, H., Chiu, Y., Kingsley, C.V., Fry, D., Delaney, S.N., Wei, S.C., Zhang, J., Maitra, A., and Yee, C. (2020). Combination of PD-1 inhibitor and OX40 agonist induces tumor rejection and immune memory in mouse models of pancreatic cancer. Gastroenterology *159*, 306–319.e12.

Mall, C., Sckisel, G.D., Proia, D.A., Mirsoian, A., Grossenbacher, S.K., Pai, C.C.S., Chen, M., Monjazeb, A.M., Kelly, K., Blazar, B.R., and Murphy, W.J. (2016). Repeated PD-1/PD-L1 monoclonal antibody administration induces fatal xenogeneic hypersensitivity reactions in a murine model of breast cancer. OncoImmunology *5*, e1075114.

McDavid, A., Finak, G., and Yajima, M. (2021). MAST: Model-Based Analysis of Single Cell Transcriptomics. R Package Version 1.18.0. https://github.com/RGLab/MAST/.

Messenheimer, D.J., Jensen, S.M., Afentoulis, M.E., Wegmann, K.W., Feng, Z., Friedman, D.J., Gough, M.J., Urba, W.J., and Fox, B.A. (2017). Timing of PD-1 blockade is critical to effective combination immunotherapy with anti-OX40. Clin. Cancer Res. *23*, 6165–6177.

Miller, B.C., Sen, D.R., Al Abosy, R., Bi, K., Virkud, Y.V., LaFleur, M.W., Yates, K.B., Lako, A., Felt, K., Naik, G.S., et al. (2019). Subsets of exhausted CD8 + T cells differentially mediate tumor control and respond to checkpoint blockade. Nat. Immunol. *20*, 326–336.

Murphy, J.T., Burey, A.P., Beebe, A.M., Gu, D., Presta, L.G., Merghoub, T., and Wolchok, J.D. (2014). Anaphylaxis caused by repetitive doses of a GITR agonist monoclonal antibody in mice. Blood *123*, 2172–2180.

Nencioni, A., Caffa, I., Cortellino, S., and Longo, V.D. (2018). Fasting and cancer: molecular mechanisms and clinical application. Nat. Rev. Cancer *18*, 707–719.

Nissen, N.I., Karsdal, M., and Willumsen, N. (2019). Collagens and Cancer associated fibroblasts in the reactive stroma and its relation to Cancer biology. J. Exp. Clin. Cancer Res. *38*, 115.

Ohshima, Y., Yang, L.-P., Uchiyama, T., Tanaka, Y., Baum, P., Sergerie, M., Hermann, P., and Delespesse, G. (1998). OX40 costimulation enhances IL-4 expression at priming and promotes the differentiation of naive human CD4! T cells into high IL-4-producing effectors. Blood *92*, 3338–3345.

Pang, Z., Chong, J., Zhou, G., de Lima Morais, D.A., Chang, L., Barrette, M., Gauthier, C., Jacques, P.É., Li, S., and Xia, J. (2021). MetaboAnalyst 5.0: narrowing the gap between raw spectra and functional insights. Nucleic Acids Res. *49*, W388–W396.

Peng, D.H., Rodriguez, B.L., Diao, L., Chen, L., Wang, J., Byers, L.A., Wei, Y., Chapman, H.A., Yamauchi, M., Behrens, C., et al. (2020). Collagen promotes anti-PD-1/PD-L1 resistance in cancer through LAIR1-dependent $CD8^+$ T cell exhaustion. Nat. Commun. *11*, 4520.

Piconese, S., Valzasina, B., and Colombo, M.P. (2008). OX40 triggering blocks suppression by regulatory T cells and facilitates tumor rejection. J. Exp. Med. *205*, 825–839.

Pietrocola, F., Pol, J., Vacchelli, E., Rao, S., Enot, D.P., Baracco, E.E., Levesque, S., Castoldi, F., Jacquelot, N., Yamazaki, T., et al. (2016). Caloric restriction mimetics enhance anticancer immunosurveillance. Cancer Cell *30*, 147–160.

Raffaghello, L., Lee, C., Safdie, F.M., Wei, M., Madia, F., Bianchi, G., and Longo, V.D. (2008). Starvation-dependent differential stress resistance protects normal but not cancer cells against high-dose chemotherapy. Proc. Natl. Acad. Sci. USA *105*, 8215–8220.

Richardson, J.R., Schöllhorn, A., Gouttefangeas, C., and Schuhmacher, J. (2021). CD4+ T cells: multitasking cells in the duty of cancer immunotherapy. Cancers *13*, 596.

Sade-Feldman, M., Yizhak, K., Bjorgaard, S.L., Ray, J.P., de Boer, C.G., Jenkins, R.W., Lieb, D.J., Chen, J.H., Frederick, D.T., Barzily-Rokni, M., et al. (2018). Defining T cell states associated with response to checkpoint immunotherapy in melanoma. Cell *175*, 998–1013.e20.

Sangaletti, S., Tripodo, C., Sandri, S., Torselli, I., Vitali, C., Ratti, C., Botti, L., Burocchi, A., Porcasi, R., Tomirotti, A., et al. (2014). Osteopontin shapes immunosuppression in the metastatic niche. Cancer Res. *74*, 4706–4719.

Shrimali, R.K., Ahmad, S., Verma, V., Zeng, P., Ananth, S., Gaur, P., Gittelman, R.M., Yusko, E., Sanders, C., Robins, H., et al. (2017). Concurrent PD-1 blockade negates the effects of OX40 agonist antibody in combination immunotherapy through inducing T-cell apoptosis. Cancer Immunol. Res. *5*, 755–766.

Siddiqui, I., Schaeuble, K., Chennupati, V., Fuertes Marraco, S.A., Calderon-Copete, S., Pais Ferreira, D., Carmona, S.J., Scarpellino, L., Gfeller, D., Pradervand, S., et al. (2019). Intratumoral Tcf1 + PD-1 + CD8 + T cells with stem-like properties promote tumor control in response to vaccination and checkpoint blockade immunotherapy. Immunity *50*, 195–211.e10.

Silva-Santos, B., Mensurado, S., and Coffelt, S.B. (2019). $\gamma\delta$ T cells: pleiotropic immune effectors with therapeutic potential in cancer. Nat. Rev. Cancer *19*, 392–404.

Stuart, T., Butler, A., Hoffman, P., Hafemeister, C., Papalexi, E., Mauck, W.M., 3rd, Hao, Y., Stoeckius, M., Smibert, P., and Satija, R. (2019). Comprehensive integration of single-cell data. Cell *177*, 1888–1902.e21.

Stüber, E., Neurath, M., Calderhead, D., Perry Fell, H., and Strober, W. (1995). Crosslinking of OX-40 ligand, a member of the TNF/NGF cytokine family, induces proliferation and differentiation in murine splenic B cells. Immunity *2*, 507–521.

Suntharalingam, G., Perry, M.R., Ward, S., Brett, S.J., Castello-Cortes, A., Brunner, M.D., and Panoskaltsis, N. (2006). Cytokine storm in a phase 1 trial of the anti-CD28 monoclonal antibody TGN1412. N. Engl. J. Med. *355*, 1018–1028.

Tan, L., Sandrock, I., Odak, I., Aizenbud, Y., Wilharm, A., Barros-Martins, J., Tabib, Y., Borchers, A., Amado, T., Gangoda, L., et al. (2019). Single-cell transcriptomics identifies the adaptation of Scart1+ Vγ6+ T cells to skin residency as activated effector cells. Cell Rep. *27*, 3657–3671.e4.

Topalian, S.L., Hodi, F.S., Brahmer, J.R., Gettinger, S.N., Smith, D.C., McDermott, D.F., Powderly, J.D., Carvajal, R.D., Sosman, J.A., Atkins, M.B., et al. (2012). Safety, activity, and immune correlates of anti-PD-1 antibody in cancer. N. Engl. J. Med. *366*, 2443–2454.

Veglia, F., Hashimoto, A., Dweep, H., Sanseviero, E., De Leo, A., Tcyganov, E., Kossenkov, A., Mulligan, C., Nam, B., Masters, G., et al. (2021). Analysis of classical neutrophils and polymorphonuclear myeloid- derived suppressor cells in cancer patients and tumor-bearing mice. J. Exp. Med. *218*, e20201803.

Vodnala, S.K., Eil, R., Kishton, R.J., Sukumar, M., Yamamoto, T.N., Ha, N.H., Lee, P.H., Shin, M., Patel, S.J., Yu, Z., et al. (2019). T cell stemness and dysfunction in tumors are triggered by a common mechanism. Science *363*, eaau0135.

Wei, M., Brandhorst, S., Shelehchi, M., Mirzaei, H., Cheng, C.W., Budniak, J., Groshen, S., Mack, W.J., Guen, E., Di Biase, S., et al. (2017). Fasting-mimicking diet and markers/risk factors for aging, diabetes, cancer, and cardiovascular disease. Sci. Transl. Med. *9*, eaai8700.

Wei, S.C., Duffy, C.R., and Allison, J.P. (2018). Fundamental mechanisms of immune checkpoint blockade therapy. Cancer Discov. *8*, 1069–1086.

Weinberg, A.D., Rivera, M.M., Prell, R., Morris, A., Ramstad, T., Vetto, J.T., Urba, W.J., Alvord, G., Bunce, C., and Shields, J. (2000). Engagement of the OX-40 receptor in vivo enhances antitumor immunity. J. Immunol. *164*, 2160–2169.

Weng, M.L., Chen, W.K., Chen, X.Y., Lu, H., Sun, Z.R., Yu, Q., Sun, P.F., Xu, Y.J., Zhu, M.M., Jiang, N., et al. (2020). Fasting inhibits aerobic glycolysis and proliferation in colorectal cancer via the Fdft1-mediated AKT/mTOR/HIF1α pathway suppression. Nat. Commun. *11*, 1869.

Wisdom, A.J., Mowery, Y.M., Hong, C.S., Himes, J.E., Nabet, B.Y., Qin, X., Zhang, D., Chen, L., Fradin, H., Patel, R., et al. (2020). Single cell analysis reveals distinct immune landscapes in transplant and primary sarcomas that determine response or resistance to immunotherapy. Nat. Commun. *11*, 6410.

Xie, X., Shi, Q., Wu, P., Zhang, X., Kambara, H., Su, J., Yu, H., Park, S.Y., Guo, R., Ren, Q., et al. (2020). Single-cell transcriptome profiling reveals neutrophil heterogeneity in homeostasis and infection. Nat. Immunol. *21*, 1119–1133.

Yang, K., Blanco, D.B., Chen, X., Dash, P., Neale, G., Rosencrance, C., Easton, J., Chen, W., Cheng, C., Dhungana, Y., et al. (2018). Metabolic signaling directs the reciprocal lineage decisions of $\alpha\beta$ and $\gamma\delta$ T cells. Sci. Immunol. *3*, eaas9818.

Zappia, L., and Oshlack, A. (2018). Clustering trees: a visualization for evaluating clusterings at multiple resolutions. GigaScience *7*, giy083.

Zhang, X., Lan, Y., Xu, J., Quan, F., Zhao, E., Deng, C., Luo, T., Xu, L., Liao, G., Yan, M., et al. (2019). CellMarker: a manually curated resource of cell markers in human and mouse. Nucleic Acids Res. *47*, D721–D728.

Zheng, G.X.Y., Terry, J.M., Belgrader, P., Ryvkin, P., Bent, Z.W., Wilson, R., Ziraldo, S.B., Wheeler, T.D., McDermott, G.P., Zhu, J., et al. (2017). Massively parallel digital transcriptional profiling of single cells. Nat. Commun. *8*, 14049.

Zheng, X., Fang, Z., Liu, X., Deng, S., Zhou, P., Wang, X., Zhang, C., Yin, R., Hu, H., Chen, X., et al. (2018). Increased vessel perfusion predicts the efficacy of immune checkpoint blockade. J. Clin. Invest. *128*, 2104–2115.

Zhu, Y., Knolhoff, B.L., Meyer, M.A., Nywening, T.M., West, B.L., Luo, J., Wang-Gillam, A., Goedegebuure, S.P., Linehan, D.C., and DeNardo, D.G. (2014). CSF1/CSF1R blockade reprograms tumor-infiltrating macrophages and improves response to T-cell checkpoint immunotherapy in pancreatic cancer models. Cancer Res. *74*, 5057–5069.

STAR★METHODS

KEY RESOURCES TABLE

REAGENT or RESOURCE	SOURCE	IDENTIFIER
Antibodies		
CD3e BV785 clone 145-2C11	Biolegend	Cat#100355; RRID: AB_2565969
CD8a Pe-Cy7 clone 2,43	TONBO biosciences	Cat# 60-1886; RRID: AB_2621862
CD45 BV510 clone 30-F11	BD Biosciences	Cat# 563891; RRID: AB_2734134
CD25 FITC clone 3C7	Biolegend	Cat# 101907; RRID: AB_961210
CD4 BV650 clone RM4-5	BD Biosciences	Cat# 740479; RRID: AB_2740204
CD279 (PD1) BV711 clone J43	BD Biosciences	Cat # 744547; RRID: AB_2742318
CD49b FITC clone DX5	eBioscience	Cat# 108905; RRID: AB_313412
GzmB PE clone QA16A02	Biolegend	Cat# 372207; RRID: AB_2687031
CD134 (OX40) PE clone OX-86	eBioscience	Cat# 12-1341-82; RRID: AB_465854
Foxp3 PerCP-Cy5.5 clone R16-715	BD Biosciences	Cat# 563902; RRID: AB_2630318
TCR γδ PE clone GL3	BD Biosciences	Cat# 553178; RRID: AB_394689
Ki67 APC clone SolA15	eBioscience	Cat# 17-5698-82; RRID: AB_2688057
CD11b PE clone M1/70	TONBO biosciences	Cat# 50-0112-U025
CD11c PerCP-Cy5.5 clone HL3	BD Biosciences	Cat# 560584; RRID: AB_1727422
F4/80 Pe-Cy7 clone BM8	eBioscience	Cat# 25-4801-82; RRID:AB_469653
CD206 AF 488 clone C068C2	Biolegend	Cat# 141709; RRID: AB_10933252
Gr1 APC clone RB6-8C5	eBioscience	Cat# 17-5931-82; RRID: AB_10933252
Ly6c BV421 AL-21	BD Biosciences	Cat# 562727; RRID: AB_2737748
CD274 (PDL1) BV711 clone MIH5	BD Biosciences	Cat# 563369; RRID: AB_2738163
CTLA4 BV421 clone UC10-4B9	Biolegend	Cat#106311; RRID: AB_10901170
Tox PE clone REA473	Miltenyi Biotec	Cat# 130-120-716; RRID: AB_2801780
IFNγ PE-CF594 Clone XMG1.2	BD Biosciences	Cat# 562333; RRID: AB_11154588
CD39 PE/Dazzle™ 594 clone Duha59	Biolegend	Cat#143811; RRID: AB_2750321
TCF-7/TCF-1	BD Biosciences	Cat# 566693; RRID: AB_ 2869823
anti-mouse OX40 (CD134)	BioXcell	Cat# BE0031; RRID: AB_1107592
anti-mouse PD-L1 (B7-H1)	BioXcell	Cat# BE0101; RRID: AB_10949073
DyLight 488 tomato lectin	Vector Labs	Cat# DL-1174-1; RRID: AB_2336404
anti-CD31 antibody	Abcam	Cat# AB28364; RRID: AB_726362
anti-CD31/PECAM-1	RD system	Cat# AF3628; RRID: AB2161028
anti-alfa-NG2	Merck Millipore	Cat# AB5320; RRID: AB_91789
Anti- CD8α (D4W2Z) XP	CST	Cat# 98941; RRID: AB_2756376
Anti-CD93	R&D	Cat#AF1696; RRID: AB_354937
Anti-BB220 clone RA3-6B2	eBioscience	Cat#36-0452-85; RRID: AB_469753
Anti_CD3 (E4T1B) XP	CST	Cat# 78588; RRID: AB_2889902
Anti TER119	Abcam	Cat# AB91113; RRID: AB_2050384
Anti MPO	Abcam	Cat# AB208670; RRID: AB_2864724
Critical commercial assays		
Tumor Dissociation Kit, mouse	Miltenyi Biotec	130-096-730
CD45 (TIL) MicroBeads, mouse	Miltenyi Biotec	130-110-618
Cell Activation Cocktail with Brefeldin A	Biolegend	423303
Software and algorithms		
Snakemake	Mölder et al. (2021)	https://github.com/snakemake/snakemake
Seurat v3.1.4	Stuart et al. (2019)	https://satijalab.org/seurat

(*Continued on next page*)

Continued

REAGENT or RESOURCE	SOURCE	IDENTIFIER
scDblFinder	Germain (2021)	https://github.com/plger/scDblFinder
SingleR (version 1.4.1)	(Aran et al., 2019)	https://github.com/LTLA/SingleR
MAST: Model-based Analysis of Single Cell Transcriptomics	McDavid et al. (2021)	https://github.com/RGLab/MAST/
ComplexHeatmap	(Gu et al., 2016)	https://www.bioconductor.org/packages/release/bioc/html/ComplexHeatmap.html
EnhancedVolcano: Publication-ready volcano plots with enhanced coloring and labeling.	Blighe et al. (2021)	https://github.com/kevinblighe/EnhancedVolcano
Metaboanalyst 5	Pang et al. (2021)	https://www.metaboanalyst.ca
GraphPad Prism	GraphPad	https://www.graphpad.com
Deposited data		
scRNA data	This paper	https://doi.org/10.17632/cy6hz8gzh9.2
Metabolomic data	This paper	https://doi.org/10.17632/cy6hz8gzh9.2
FACS data	This paper	https://doi.org/10.17632/cy6hz8gzh9.2

RESOURCE AVAILABILITY

Lead contact

Further information and requests for resources and reagents should be directed to and will be fulfilled by the Lead Contact, Valter D Longo (vlongo@usc.edu, valter.longo@ifom.eu).

Materials availability

This study did not generate new unique reagents.

Data and code availability

The scRNA sequencing data, metabolomic data and FACS data have been deposited in the Mendley Data and are publicly available as of the date of publication. The DOI is listed in the key resources table.

This paper does not report original code.

Any additional information required to reanalyze the data reported in this paper is available from the lead contact upon request.

EXPERIMENTAL MODEL AND SUBJECT DETAILS

Tumor cell lines

The 4T1 tumor cells were obtained from ATCC, while TS/A cell was purchased by Merck Millipore. Cells were grown in RPMI1640 or DMEM supplemented with 10% fetal bovine serum (FBS), 2 mM L-glutamine, penicillin (100 U ml−1) and streptomycin (100 μg mL−1) at 37°C with 5% CO2 and maintained at a confluence of 70–80%.

Mice

NSG and BALB/c female mice, 6–8 weeks old, were purchased from Charles River and housed under pathogen-free conditions in Cogentech animal facility and with food and water ad libitum. All procedures were carried out in accordance with approved by Institutional Animal Care and Use Committee (OPBA) animal protocols at IFOM-the FIRC Institute of Molecular Oncology and by Italian Ministry of Health (authorization 674_2019).

METHOD DETAILS

Tumor implantation, immune checkpoint blockade (ICB) treatment, and tumor volume measurement

For triple negative breast cancer (TNBC) model, 10^4 4T1 or 10^5 TS/A cells were injected orthotopically into mammary fat pad of 6–8 week old BALB/c or NSG mice.

Four days after tumor injection, mice were treated with anti-OX40 (100 μg per mouse) or anti-PD-L1 (100 μg per mouse) every other day for three time. The combined treatment was administered sequentially. The mice were treated with anti-OX40 the first week, while the second week with anti-PD-L1. The mice underwent 2 cycles of FMD starting the third day after tumor implantation. 1 FMD cycle consists of alternating 4 consecutive days of fasting mimicking diet and 3 days of refeeding with standard diet. FMD components are described in Brandhorst et al., (2015), and Di Biase et al., (2016) (Brandhorst et al., 2015; Di Biase et al., 2016).

Tumors were measured every 3–4 days using a digital caliper; tumor volume was calculated using the formula V = (L × W x H)/2, where V is tumor volume, L is the length of the tumor (longer diameter), W is the width of the tumor (shorter diameter) and H is the height (diameter of tumor perpendicular to length and width). Mice were monitored for tumor growth and survival.

To assess the immune related adverse events, the following procedure was implemented: on day 3 after implantation of 4T1 tumor cells in the mammary fat pad, mice underwent FMD cycles (4 days) and were treated with IgG, anti-PD-L1, and anti-OX40 (100μg/mouse) on days 4, 6 and 8. The following week, on day 13 and after 3 days of refeeding with the standard diet, mice were fed FMD and treated with IgG, anti-PD-L1, and anti-OX40 (100μg/mouse). The mice undergoing the combined therapy were treated with anti-OX40 on days 4, 6 and 8 and with anti-PD-L1 on days 11, 13 and 15. At week 3, mice underwent cycle 3 of FMD and treated with IgG, anti-PD-L1 and anti-OX40 on day 21 (last day of fasting).

Flow cytometry analysis of tumor-infiltrating lymphocytes and apoptosis

Leukocyte infiltration in tumor samples was evaluated, as previously described (Sangaletti et al., 2014), using the following antibodies: CD45; Gr-1; CD11b; F4/80, Ly6C, CD49b, PD-L1, CD4, CD8, CD3, TCR gd, CD206, OX40, CD25 and PD-1 (from eBioscience, Becton Dickinson and Biolegend). For intracellular markers, after surface staining, cells were fixed, permeabilized and stained with FOXP3, GzmB or Ki-67 antibodies according to manufacturer instruction (eBioscience). Samples were acquired using a BD LSR II Fortessa instrument and analyzed with FlowJo software (TreeStar). T cells were activated using Cell Activation Cocktail with Brefeldin A (Biolegend. # 423,303), following the manufacturer's protocol.

Specific antibodies used for flow cytometry analyses are listed in Table S1.

Complete blood counts

Complete blood counts were performed using AcT 5 diff Hematology Analyzer (Beckman Coulter) in accordance to manufacturer's protocol. In brief, blood was collected from the tail vein and immediately 20 μL of blood was diluted in 100 μL of Sodium Citrate solution and whole blood parameters were evaluated.

Immunohistochemistry

Tumors and tissues were dissected from mice and fixed in 4% parformaldehyde overnight. Samples were dehydrated, and embedded in paraffin, then four-micrometres-thick sections were cut, stained for Haematoxylin/Eosin (Diapath) according to standard protocol and mounted in Eukitt (Bio-Optica). Picrosirius red staining (Scy Tek Lab, SRS-IFU) was performed to selectively visualize collagen I and III fibers under a bright-field microscope and under a polarized light, whereas the toluidine blue staining (Sigma, CI 52040) was used to detect mast cells.

For Immunohistochemical and immunofluorescence staining, paraffin was removed with xylene and the sections were rehydrated in graded alcohol. Antigen retrieval was carried out using preheated target retrieval solution for 30 min. Tissue sections were blocked with FBS serum in PBS for 60 min and incubated overnight with primary antibodies reported in Table S1. The antibody binding was detected using a polymer detection kit (GAM-HRP, Microtech) followed by a diaminobenzidine chromogen reaction (Peroxidase substrate kit, DAB, SK-4100; Vector Lab). All sections were counterstained with Mayer's hematoxylin and visualized using a bright-field microscope.

For double immunofluorescence, tumor sections were incubated ON with primary antibodies and incubated with corresponding secondary antibodies Alexa Fluor 488, 594, or 647 (1:200, Molecular Probes, Invitrogen Life Technologies, Grand Island, New York) for 1 h at room temperature. To visualize the cell nuclei, human specimens were counterstained with 4,6-diamidino-2-phenylindole (DAPI, Sigma-Aldrich), mounted with a Phosphate-Buffered Salines/glycerol solution and examined under a Leica TCS SP2 confocal microscope.

Preparation of single-cell suspension

For each condition two mice were scarified for the scRNA in order to have a biological duplicate for each condition and a total of eight scRNA sequencing reactions.

Tumor were harvested and dissociated using the Miltenyi Biotec tumor dissociation kit (mouse, tough tumor dissociation protocol) for 40 min at 37°C. Cell suspension were filtered through 70 μm strainer and the leukocytes were isolated by density separation using lympholyte M-cell separation media. Tumor infiltrating leukocytes were further enriched by incubation with CD45 (TIL) MicroBeads according to manufacturing protocol. CD45+ cells from the eluted fraction were resuspended in PBS with 0.04% BSA at a concentration of 1000 cells/μL for single cell RNA sequencing.

Droplet-based single-cell sequencing

The cell resuspension was loaded on GemCode Single Cell instrument (10x Genomics) to generate single-cell beads in emulsion and scRNA-seq libraries were prepared using the Chromium Single Cell 3′ Reagent Kits The libraries were sequenced using an Illumina Novaseq 6000 sequencer with pair-end 150 bp reading strategy.

Vascular perfusion

Vascular perfusion was determined by injecting DyLight 488 tomato lectin (100 μL, Vector Lab) into the tail vein of BALB/c mice 10 min before the sacrifice. Tumor were fixed in 1% paraformaldehyde (PFA) overnight at 4°C, transferred to 30% sucrose solution overnight

at 4°C and finally embedded in OCT. The 10 μm thick cryosections were incubated with anti-CD93 and detected by AF 568 conjugated anti-rat antibody. The sections were counterstained with DAPI.

Sample preparation for metabolomic analysis

Tumor masses (5 biological samples for each condition) were collected at the experiment endpoint and processed by MS-Omics. The tumor masses were mixed with methanol/water (1:2), homogenized with stainless steel beads and ultrasonicated for 5 min. After centrifugation of the tubes the supernatant were collected, and the pellet were reextracted by adding a new portion of methanol/water and repeating the process described above. The two supernatant aliquots were pooled, splitted into two HPLC vials and dried under a gentle nitrogen flow. The samples were reconstituted with 6 x the sample with water. The samples analysis was carried out using Thermo Scientific Vanquish LC coupled to Thermo Q Exactive HF MS. An electrospray ionization interface was used as ionization source. Analysis was performed in negative and positive ionization mode. The UPLC was performed using a slightly modified version of the protocol described Hsiao et al., 2018 (https://doi.org/10.1021/acs.analchem.8b02100).

QUANTIFICATION AND STATISTICAL ANALYSIS

All the data are presented as mean ± SEM and are plotted using GraphPad Prism software. The p value was calculated using ANOVA or unpaired T test or Log rank [Mantel-Cox] test. Only p values <0.05 were considered statistically significant. Each experiment was repeated at least 3 times with 3 or more samples (n) for each condition. Information about specific statistic test employed and the exact value of n (e.g., biological replicates, number of animals, etc) are reported in the Results or figure legends.

ScRNA data pre-processing and clustering

FASTQ files for each condition were converted to count matrixes using a singularity-conda- dependent Snakemake pipeline (Mölder et al., 2021) which exploits the count command of CellRanger (v5.0.0) and the mouse reference genome mm10-2020-A version.

Count matrixes were merged using Seurat v3.1.4 (Stuart et al., 2019), number of cells was verified to be higher than 900 cells per condition, and doublets were filtered out with scDblFinder (Germain, 2021). Cells with less than 500 and more than 5,000 transcripts, less than 250 genes, less than 0.80 of novelty score (log10Genes/UMI), and less than 0.20 of mitochondrial gene ratio were removed. Moreover, genes expressed in less than 5 cells were removed as well. We checked for both batch effect and cellular phase gene expression and we evaluated that no integration was required. We applied sctransform normalization using SCTransform() function in Seurat and regressed out of percentage of mitochondrial genes. We perform principal component analysis (PCA) on the normalized (SCT) assay and we run the Uniform Manifold Approximation and Projection (UMAP) using the function runUMAP().

We applied the graph-based clustering approach of Seurat using FindNeighbours() and FindClusters() functions and the first 15 principal components, evaluated with the elbow plot method. The resolution of the clusters was evaluated by visual inspection and a value equal to 0.80 was chosen as the best result.

Cell type annotation and cluster name assignation

We used an automated method for cell assignation (Aran et al., 2019) using as reference the microarray profiles of ImmGen() (Heng and Painter, 2008) and the default delta threshold, label names were manually curated in order to have the best granularity. We confirmed the results using two web servers (Heng and Painter, 2008; Zhang et al., 2019) and known gene marker expression. According to the percentage of cell populations in each cluster we assigned a name to each cluster, when more than one cell population was highly represented in a cluster, we assigned a composite name in descending percentage order and separated by an underscore. When the same name was assigned to more clusters an alphanumeric code was added at the end of the name.

Subclustering

Cells in the macro-clusters of interest (T cells and Neutrophils) were extracted using subset() function and the filtered counts were normalized as before. PCA was performed and in this case the function maxLikGlobalDimEst() function of the package intrinsicDimension (Johnsson et al., 2015) was used to evaluate the best number of principal components to use for the clustering workflow as suggested by Germain et al., (2020) (Germain et al., 2020). Clustering was performed as above and the best resolution was evaluated with clustree package (Zappia and Oshlack, 2018) that allows to see how each cluster is connected to the others with different resolutions and when a stability is reached. The resolutions of 0.3 and 0.2 were chosen respectively for T cells and Neutrophils subclustering.

The sub-clusters name assignation was performed evaluating the gene expression of pivotal markers for the identification of subcellular populations in cancer models as in Wisdom et al., (2020), Xie et al. (2020), Veglia et al., (2021) (Wisdom et al., 2020; Xie et al., 2020; Veglia et al., 2021). Violin and UMAP plots used to evaluated the gene expression were generated using slightly modified functions of Seurat package and exploit the information of the normalized count matrix.

Differential expression gene analysis

Dot plots were generated using and in-house R function that takes advantage of the information of the top 20 differentially expressed genes (DEG) in only the cells of that specific cluster retrieved by FindAllMarkers() function of Seurat package using the information of

the 'RNA' assay, a hurdle model tailored to scRNA-seq data (McDavid et al., 2021), a minimum percentage of cells equal to 25% and threshold for logFC equal to log(1.5).

To build the heatmap, we used the ComplexHeatmap package function (Gu et al., 2016) and we used the top 40 DEG retrieved as for the dot plot.

Volcano plot were generated using EnhancedVolcano package (Blighe et al., 2021) which exploited the information of DEG between the conditions tested. DEG were extracted using FindMarkers() function with minimum percentage of cells equal to 25% and logFC threshold equal to zero after removing mitochondrial and ribosomal genes. FC was converted in log2 FC and used to build the volcano plot.

Metabolomic data analysis

The raw GC-MS data were pre-processed using Metaboanalyst 5 (Pang et al., 2021) and the experimental data were normalized by the total spectral intensity. Tumor metabolic profiles were analyzed by partial least squares-discriminate analysis (PLS-DA) and depicted in the heatmap cluster plot of peak intensities of significantly different intracellular metabolites ($p \leq 0.05$) between fasting mimicking and standard diet. The quantitative metabolic pathway enrichment analysis was performed on statistically significant metabolites by using MetaboAnalyst 5 enrichment analysis software. The difference of quantitative analysis results between the two groups was analyzed by GraphPad Prism 8 (*t* test, $p < 0.05$).

Morphometric analysis

Measurements of blood vessels density were performed using ImageJ software. For each tumor, 3 sections were prepared at distance of 100 μm from each other and 5–10 microphotographs were collected using Olympus BX63 Upright microscope equipped with a motorized stage Black and white camera: Hamamatsu Orca AG (12 bit, 6.45 um pixel size) and Color Camera: Leica DFC450C (36 bit, 3.4 um pixel size).$CD93^+$ or Tomato $lectin^+$ area per random field was calculated in peri- and intratumoral regions. Statistical analyses were performed using GraphPad Prism 7.0 software (Anon., n.d.).